FABRICATION AND CHARACTERIZATION OF ZINC OXIDE BASED SURFACE ACOUSTIC WAVE DEVICES

A THESIS
SUBMITTED TO MATERIALS SCIENCE AND
NANOTECHNOLOGY PROGRAM
OF THE GRADUATE SCHOOL OF ENGINEERING AND SCIENCE
OF BILKENT UNIVERSITY
IN PARTIAL FULFILLMENT OF THE REQUIREMENTS
FOR THE DEGREE OF
MASTER OF SCIENCE

By
Mehmet Alican Noyan
August, 2013

I certify that I have read this thesis and that in my opinion it is fully adequate, in scope and in quality, as a thesis for the degree of Master of Science.

____

Assist. Prof. Dr. Necmi Bıyıklı (Advisor)

I certify that I have read this thesis and that in my opinion it is fully adequate, in scope and in quality, as a thesis for the degree of Master of Science.

____

Assist. Prof. Dr. Çağlar Elbüken

I certify that I have read this thesis and that in my opinion it is fully adequate, in scope and in quality, as a thesis for the degree of Master of Science.

____

Assoc. Prof. Dr. H. Emrah Ünalan

Approved for the Graduate School of Engineering and Science:

____

Prof. Dr. Levent Onural
Director of Graduate School

ABSTRACT

FABRICATION AND CHARACTERIZATION OF ZINC OXIDE BASED SURFACE ACOUSTIC WAVE DEVICES

Mehmet Alican Noyan

M.S. in Materials Science and Nanotechnology

Advisor: Assist. Prof. Dr. Necmi Bıyıklı

August, 2013

Surface acoustic wave (SAW) devices, as applied to today's technology, were first described in 1965. Since then, these devices were applied to a wide variety of fields. Bandpass filter is their most common application, which is an important component in consumer products such as televisions and mobile phones. SAW devices can also be utilized as chemical and biological sensors. Driving force behind the development of SAW sensors is their small size, high sensitivity, reliability, and durability.

This thesis presents the development and characterization of ZnO/Si based SAW devices. ZnO thin films with c-axis orientation were deposited using rf-magnetron sputtering. Effect of post deposition annealing on the structure of ZnO and on the SAW device performance was studied. It was found that annealing ZnO above $600^{o}C$ is detrimental for SAW device performance. Surface roughness of ZnO increases as the annealing temperature increases. In literature, roughness increase is presented as one of the reasons behind device breakdown. This work shows that roughness is not the primary cause for the breakdown. In addition, effect of SiO_2 interlayer insertion between ZnO/Si structure on the device performance was examined together with the effect of ZnO thickness.

Keywords: Surface acoustic wave (SAW) device, Zinc oxide (ZnO), Sputtering, Post-deposition annealing

ÖZET

ÇİNKO OKSİT TEMELLİ YÜZEY AKUSTİK DALGA AYGITLARININ GELİŞTİRİLMESİ VE NİTELENDİRİLMESİ

Mehmet Alican Noyan
Malzeme Bilimi ve Nanoteknoloji, Yüksek Lisans
Tez Yöneticisi: Yrd. Doç. Dr. Necmi Bıyıklı
Ağustos, 2013

Bugün bildiğimiz anlamda kullanılan yüzey akustik dalga (SAW) aygıtları, ilk olarak 1965'te tanıtıldı. Televizyon ve cep telefonu gibi tüketici ürünlerinde kullanılan band geçiren filtreler bu cihazların en yaygın kullanım alanıdır. SAW aygıtlar ayrıca kimyasal ve biyolojik algılayıcı olarak da kullanılabilir. SAW algılayıcı geliştirmenin arkasında yatan temel neden bu cihazların küçük boyutlu, yüksek hassasiyette ve dayanıklı olmalarıdır.

Bu tez ZnO/Si yapısına dayalı SAW aygıtının geliştirilmesini ve nitelendirilmesini sunmaktadır. C-eksen yönelimli ZnO ince filmler, sıçratma yöntemi ile kaplanmıştır. Kaplama sonrasında uygulanan tavlamanın ZnO yapısına ve SAW aygıt başarımına etkisi detaylı bir şekilde incelenmiştir. 600°C üzerindeki sıcaklıklarda tavlamanın SAW aygıtı olumsuz etkilediği tespit edilmiştir. ZnO'in yüzey pürüzlülüğü tavlama sıcaklığı arttıkça artmaktadır. Kaynaklar, pürüzlülük artışını aygıtın tavlama sıcaklığı artışına dayalı bozunumunun nedenlerinden biri olarak vermektedir. Bu çalışma ise bozunumun yüzey pürüzlülüğünden kaynaklanmadığını göstermektedir. Tavlamanın aygıt başarımı üzerindeki etkisine ek olarak, ZnO/Si yapısının arasına SiO_2 eklenmesinin ve ZnO kalınlığının da aygıt başarımına etkileri incelenmiştir.

Anahtar kelimeler: Yüzey akustik dalga (SAW) aygıtları, Çinko oksit (ZnO), Sıçratma, Kaplama sonrası tavlama

To my lovely sister Aslı

Acknowledgements

I would like to express my appreciation to my supervisor Assist. Prof. Dr. Necmi Bıyıklı for his guidance, encouragement and advice throughout the development of this work. I would also like to thank Assist. Prof. Dr. Çağlar Elbüken and Assoc. Prof. Dr. H. Emrah Ünalan for being in my thesis committee and sharing their useful comments.

I am grateful to İnci Dönmez for her endless support even in hard times, to Engin Çağatay for teaching me almost everything I know in the cleanroom, and to Çağla Özgit-Akgün for sharing her profound knowledge with me. Not forgetting my friends who always been there: Levent, Deniz, Feyza, Fatih, Adem, Sami, Enver, Furkan, Burak, Ayşe, Elif, Pelin, Gamze, Enes and Tahsin. I would particularly like to thank UNAM engineers Semih Yaşar, Fikret Piri and Mustafa Güler. Furthermore, I would like to thank Elif Aydoğdu, Amir Ghobadi and Çağrı Çetintepe for their help during network analyzer measurements.

I would like to express my appreciation to my uncle Prof. Dr. İsmail Cevdet Noyan for his invaluable contributions to the content of the thesis.

Finally, yet importantly, I would like to express my heartfelt thanks to my beloved family, Aslı, Aytül and Turgut Noyan for their endless support.

Contents

Chapter 1 Introduction **1**
1.1 Motivation 2
1.2 Objectives 2
1.3 Organization of the Thesis 3
Chapter 2 Theoretical Background and Literature Overview **4**
2.1 Theory of Piezoelectricity 4
2.1.1 History 4
2.1.2 Crystal Geometry 6
2.1.3 Tensors 10
2.1.4 Piezoelectricity 13
2.1.5 Derivation of the piezoelectric moduli for the point group 6mm 17
2.2 Theory of SAW devices 27
2.2.1 Theory of Operation 27
2.2.2 Surface Waves 31
2.2.3 Parameters Affecting Wave Propagation 33
2.2.4 Measurement 34
2.3 Literature Overview 34
Chapter 3 Experimental Details **37**
3.1 Device Fabrication 37
3.1.1 Substrate and Surface Preparation 38
3.1.2 SiO_2 Deposition Using RF Magnetron Sputtering 38
3.1.3 ZnO Deposition Using RF Magnetron Sputtering 39
3.1.4 Post-deposition Annealing of ZnO 40
3.1.5 Formation of Interdigitated Transducers (IDT) 41
3.1.5.1 Photolithography 41
3.1.5.2 Deposition of Titanium and Gold 44
3.1.5.3 Lift-off 45
3.2 Characterization Methods 47
3.2.1 Methods Used for ZnO Characterization 47
3.2.1.1 X-Ray Diffraction 47
3.2.1.2 X-Ray Photoelectron Spectroscopy 49

3.2.1.3 Scanning Electron Microscopy........................ 51
3.2.1.4 Transmission Electron Microscopy................. 51
3.2.1.5 Spectroscopic Ellipsometry............................. 52
3.2.1.6 Atomic Force Microscopy............................... 53
3.2.2 SAW Device Characterization..................................... 55
Chapter 4 Results and Discussion... 59
4.1 Optimization and Characterization of ZnO.................................. 59
4.1.1 Optimization of Deposition Parameters....................... 59
4.1.1.1 Deposition Temperature.................................. 60
4.1.1.2 Deposition Power.. 62
4.1.1.3 Chamber Pressure.. 63
4.1.2 Characterization of ZnO... 65
4.1.3 Post-deposition Annealing.. 69
4.2 Characterization of SAW Devices.. 76
4.2.1 Effect of Annealing.. 76
4.2.2 Effect of SiO_2 Interlayer.. 81
4.2.3 Effect of Film Thickness.. 82
Chapter 5 Conclusions and Future Directions... 83
Bibliography... 86

List of Figures

Figure 1.1: A surface acoustic wave device. 1
Figure 2.1: Unit cell which can be defined with three vectors or six scalars [10]. 7
Figure 2.2: 14 Bravais lattices [10]. 7
Figure 2.3: Operation of symmetry elements mirror plane and rotation axes [10]. 8
Figure 2.4: (a) Atomic arrangement of a hexagonal close packed structure, circles represent atoms (b) Hexagonal lattice with two atoms per lattice point. Atoms marked with x are atoms shown in (a) [10]. 9
Figure 2.5: Crystal structure of CsCl(a) [10], ZnO(b) [11]. 9
Figure 2.6: Transformation of axes. Angle between $x_1^{'}$ and x_2 is shown. 11
Figure 2.7: Ion positions in a quartz lattice with and without external stress [12]. 14
Figure 2.8: Symmetry elements of the point group 6mm. A six-fold rotation axis, two mirror planes. x_1 and x_2 axes are shown. x_3 axis is parallel to the 6-fold rotation axis, with the direction out of the page. 17
Figure 2.9: Transformation of axes by the mirror plane shown by the straight line. 18
Figure 2.10: Transformation of axes by the second mirror plane. 20
Figure 2.11: Transformation of axes due to 6-fold rotation axis....................... 22
Figure 2.12: Crystal structure and surface free energies for three different planes of ZnO [11].. 26
Figure 2.13: Interdigital transducer function on a piezoelectric material [15]... 27
Figure 2.14: Basic working principle of a SAW device. Edge view [15]. 28
Figure 2.15: Surface acoustic wave delay line with interdigitated transducer dimensions. 29
Figure 2.16: (a) Longitudinal, (b) Transverse wave [16]. 31
Figure 2.17: Shear vertical and shear horizontal vibration types [16]. 31
Figure 2.18: A schematic illustration of Rayleigh Wave [18]. 32

Figure 3.1: VAKSIS NanoD – 4S Magnetron Sputtering system which was used for SiO_2, ZnO, Ti and Au thin film depositions. 39
Figure 3.2: ATV-Unitherm (RTA SRO-704) rapid thermal annealing (RTA) system. 40
Figure 3.3: (a) Spinning of HMDS and AZ5214E were done in Laurell spinner system. (b) Precision hot plates where soft and hard-bake steps were performed. 42
Figure 3.4: Heidelberg Instruments DWL-66 Laser Mask Writer used for photomask production. 43
Figure 3.5: EVG 620 mask aligner used for the exposure of photoresist-coated wafers. 44
Figure 3.6: Microfabrication steps of SAW devices used in this work. 46
Figure 3.7: Optical microscope images of the final device showing gold electrodes over ZnO. (a) One of the interdigital transducers. (b) Finger pairs. . 47
Figure 3.8: Schematic representation of Bragg's law. 48
Figure 3.9: PANalytical X'Pert PRO Multi-Purpose X-Ray Diffractometer used for the XRD measurements 49
Figure 3.10: Schematic representation of the basic components of X-ray photoelectron spectroscopy. 50
Figure 3.11: Thermo Scientific K-Alpha X-Ray photoelectron spectroscopy system. 50
Figure 3.12: Nova-NanoSem scanning electron microscope. 51
Figure 3.13. FEI Tecnai G2 F30 transmission electron microscope. 52
Figure 3.14: J.A. Woolam Co. V-VASE spectroscopic ellipsometer. 53
Figure 3.15: Schematic representation of how tip movements are detected typically in AFM. 54
Figure 3.16: PSIA XE-100E atomic force microscope used for the morphological characterization of ZnO films. 54
Figure 3.17: Schematic two-port network. 56
Figure 3.18: A scheme showing calibration steps. The order is not important. . 57
Figure 3.19: A figure depicting each calibration step. Black square is 50 Ω. 57

Figure 3.20: Schematic illustration of the measurement. 58
Figure 3.21: Actual measurement setup showing network analyzer (E5071C) and the probe station (a), RF probes and the device under test can be seen in (b). 58
Figure 4.1: Radial scans of the 0002 reflections for the films deposited at three different temperatures... 61
Figure 4.2: Radial scans of the 0002 reflections for the films deposited under three different rf power values. 62
Figure 4.3: Radial scans of the 0002 reflections for film deposited at different chamber pressures. 64
Figure 4.4: SEM image of the (a) surface and (b) cross section of the sputtered 402 nm thick ZnO on Si wafer. 65
Figure 4.5: TEM image of the ZnO cross section. SiO_2 is the native oxide of the silicon wafer while Pt is the holder coated during sample preparation. 66
Figure 4.6: XPS depth profile analysis results of the ZnO thin film over silicon wafer showing the uniform composition throughout the bulk film.................. 67
Figure 4.7: (a) Zn 2p and (b) O 1s high resolution XPS spectra of the optimized ZnO thin film after 300 s of Ar etch.. 68
Figure 4.8: AFM image of sputtered ZnO over silicon wafer. 68
Figure 4.9: Fitting data of the ZnO film using Cauchy dispersion function to obtain thickness and refractive index values. 69
Figure 4.10: Radial scans of the 0002 reflections for the as-deposited and annealed films.. 70
Figure 4.11: RMS surface roughness values of the films annealed at different temperatures. Error values are smaller than the height of the data points.......... 72
Figure 4.12: Refractive index of the films annealed at different temperatures. Error values are smaller than the height of the data points. 73
Figure 4.13: SEM image of the ZnO surface annealed at (a) 600°C and (b) 1000°C. 74
Figure 4.14: RMS surface roughness vs. Annealing temperature graph for annealing durations 5 and 30 min.. 75

Figure 4.15: Radial scans of the 0002 reflections for the films annealed at 1000°C for 5 and 30 min. 75
Figure 4.16: Response of the SAW devices utilizing ZnO annealed at (a) 400°C for 30 min, (b) 600°C for 5 min, (c) 600°C for 30 min, (d) 800°C for 5 min, (e) 800°C for 30 min, (f) 1000°C for 5 min and (g) 1000°C for 30 min. 78
Figure 4.17: Insertion loss vs. frequency response of the devices utilizing ZnO annealed at 600°C for 5 and 30 min. 80
Figure 4.18: Effect of SiO_2 addition on SAW device response. 81
Figure 4.19: Insertion loss vs frequency response of the devices utilizing 1560 and 1890 nm thick ZnO. 82

List of Tables

Table 2.1: Restrictions imposed on d_{ijk} by the mirror plane whose normal is parallel to x_2 20

Table 2.2: Restrictions imposed on piezoelectric moduli coefficients.............. 21

Table 2.3: Resulting d_{ijk} after restrictions in Table 2.2 are applied................... 21

Table 2.4: d_{ijk} after the restrictions imposed by both mirror planes................. 21

Table 2.5: Coefficients of the piezoelectric moduli after restrictions imposed by the transformations due to symmetry elements 6, m, m.................................. 23

Table 2.6 SAW device application areas after Hickernell [25]......................... 35

Table 3.1: Optimized Sputtering Parameters for ZnO Deposition.................... 40

Table 3.2: Sputtering parameters for titanium and gold.................................. 45

Table 4.1: Integrated intensity values with respect to different deposition temperatures. 61

Table 4.2: Integrated intensities per unit thickness for different RF power values. 63

Table 4.3: Integrated intensities per unit thickness for the films deposited using three different chamber pressures.. 64

Table 4.4: ZnO deposition recipe determined for the VAKSIS RF magnetron sputtering system.. 65

Table 4.5: Integrated intensity per unit thickness and full width at half maximum values according to annealing temperatures... 70

Table 4.6: Annealing parameters for ZnO.. 77

Chapter 1

Introduction

Surface acoustic wave (SAW) devices are composed of two interdigital transducers (IDTs) fabricated on a piezoelectric material (Figure 1.1). This material can be a piezoelectric substrate or a piezoelectric thin-film over a non-piezoelectric substrate. Piezoelectric materials deform under the application of electric fields (E-fields) and form E-fields under the application of stress. A given electrical signal to the input IDT transformed to mechanical deformation in the crystal due to piezoelectricity. If this electrical signal is oscillating, then the deformation would be oscillating. Oscillating deformation causes surface acoustic waves in the solid. When this wave reaches the output IDT, it is converted back to the electrical signal. IDT dimensions allow a signal with a specific frequency to pass.

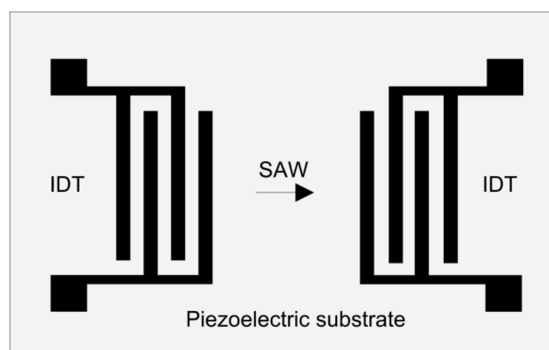

Figure 1.1: A surface acoustic wave device.

These devices are used as the frequency filters in wireless communication systems. Perturbance of the wave at the surface between the IDTs would cause attenuation and phase shifting of the electrical signal obtained at the output IDT. Inspecting the relation between the cause of the perturbance and the change in the signal resulted in the development of SAW sensors.

1.1 Motivation

SAW devices have wide range of application areas. In electronic circuitry, SAW devices can be used as oscillators, filters and transformers. Some important advantages of these devices are their small size and weight, durable structure and easy production.

SAW devices are also employed as sensors due to their unique advantages. First important advantage is the confinement of SAW energy in the surface of the device which enables the production of very high sensitive devices. In addition, dimensions of these devices are small hence they can be easily integrated into various platforms.

1.2 Objectives

In this work, SAW devices based on ZnO over silicon wafer were fabricated. The essential purpose of this work was to investigate the parameters affecting SAW device operation and optimize them for improved performance. Effects of post-deposition annealing on ZnO structure and SAW device operation were investigated in detail. In addition, influence of deposition parameters on the crystal structure of ZnO was studied. Afterwards, addition of SiO_2 interlayer between ZnO and the substrate was reported. Finally, the effect of ZnO thickness on the device performance was analyzed.

1.3 Organization of the Thesis

This part briefly explains the organization of the thesis. In Chapter 2, theory of piezoelectricity and SAW devices are presented. This part is crucial for understanding and improving device performance. Same chapter also includes a brief overview of the SAW sensor literature. In Chapter 3, fabrication of the SAW device is explained in detail. It is followed by the introduction of the experimental methods used to characterize the piezoelectric film and the SAW device. Results of these characterizations are presented and discussed in Chapter 4. Thesis concludes with Chapter 5 which gives a summary of the work presented in this thesis and possible future directions of study.

Chapter 2

Theoretical Background and Literature Overview

In this chapter, a brief history on piezoelectricity and main concepts of the piezoelectric theory will be introduced. Afterwards, ZnO will be examined in terms of its piezoelectric properties. In addition, theory of surface acoustic wave (SAW) devices will be discussed including the operation principles, surface waves, parameters affecting wave propagation and the measurement methods. Chapter will end with a brief literature overview on SAW devices.

2.1 Theory of Piezoelectricity

2.1.1 History

Piezoelectricity literally means electricity caused by pressure where 'piezo' means press in Greek. From a scientific point of view, piezoelectricity is defined by Cady [1] as follows, "electric polarization produced by mechanical strain in crystals belonging to certain classes, the polarization being proportional to the strain and changing sign with it." Actually this is the definition of direct piezoelectric effect. When subject to electrical polarization, a piezoelectric crystal becomes mechanically strained. This is called the converse piezoelectric

effect. The direct piezoelectric effect is named as 'direct' only because it is realized before the converse piezoelectric effect.

Curie brothers, Pierre and Jacques Curie, have been credited for the discovery of piezoelectricity in 1880, although piezoelectricity was observed before their work. Here, it is convenient to quote the introduction paragraphs of their paper [1], [2] in which they announced their discovery, in translation:

"Those crystals having one or more axes whose ends are unlike, that is to say hemihedral crystals with oblique faces, have the special physical property of giving rise to two electric poles of opposite signs at the extremities of these axes when they are subjected to a change in temperature: this is the phenomenon known under the name of pyroelectricity.

We have found a new method for the development of polar electricity in these same crystals, consisting in subjecting them to variations in pressure along their hemihedral axes"

Wilhelm Gottlieb Hankel, a senior experimental physicist, dealed with this new effect and could not find a general correlation between this new phenomenon and pyroelectricity; hence, Hankel claimed it is an independent phenomenon and proposed the name 'piezoelectricity' for this new effect [3]. In 1881, Gabriel Lippmann examined piezoelectricity in terms of thermodynamic principles and concluded that there should be a reverse effect [4]. Later that year Curie brothers verified the statement [5].

In 1890s, Lord Kelvin constructed the theory of piezoelectricity [6] based on thermodynamic grounds and piezoelectric formulation was handled rigorously by Woldemar Voigt [7].

It took some time for piezoelectricity to find a practical application. In 1917, Paul Langevin [8], doctoral student of Pierre Curie, showed that quartz plates could be used to emit and receive sound waves under water. Langevin developed the first sonar (abbreviation of sound navigation and ranging) using this principle. This development awakened the interest for piezoelectric devices and led to the research and development of new piezoelectric materials and new applications. Today, piezoelectricity is utilized in a wide variety of applications such as radio transmission, filter technology, nano-positioning, measurement of pressure, velocity and acceleration, gas sensors, biological sensors etc.

2.1.2 Crystal Geometry

Understanding crystals is indispensable for understanding piezoelectricity. Piezoelectricity depends on the crystal structure of the material and amorphous materials do not possess piezoelectricity (except some polymers [9]).

A crystal is a solid composed of atoms, ions or molecules in which they are arranged in an ordered pattern in three dimensions. In order to the study the periodicity of crystals, lattices are used. Lattice is a three dimensional array of points. All of these points have the same surrounding with each other and they are called as lattice points. It is critical to remember that atom sites and lattice points are different entities.

Unit cells are the cells which can be used to define the whole lattice. Vectors **a**, **b**, **c** (or six scalars a, b, c, α, β, γ) define a unit cell entirely (Figure 2.1). A unit cell defines the entire lattice.

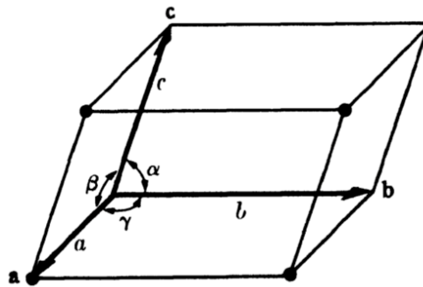

Figure 2.1: Unit cell which can be defined with three vectors or six scalars [10].

Depending on the magnitude and direction of these vectors, units cells of various shapes can occur. There are only seven different kind of crystal systems and only fourteen different point lattices which fulfill the requirement of a point lattice. These 14 point lattices are called Bravais lattices (Figure 2.2).

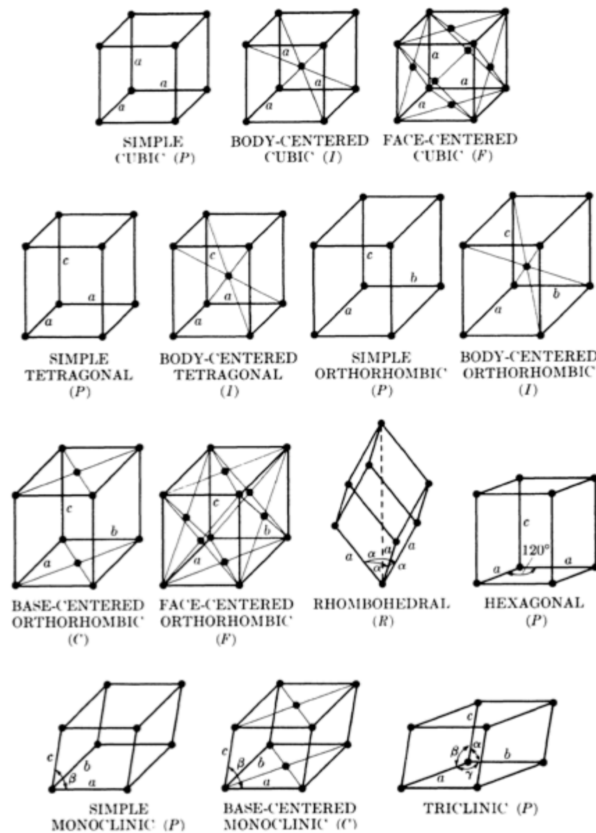

Figure 2.2: 14 Bravais lattices [10].

Crystals possess symmetry and it is a way to define crystals. If an operation performed on the crystal leaves it indistinguishable from its previous state this operation is called as symmetry operation. Elements used to define these operations are called symmetry elements. There are four symmetry operations: reflection, rotation, inversion and roto-inversion. For instance mirror plane (designated as 'm') is the symmetry element used to define reflection. Rotation axes define the operation rotation (Figure 2.3). If a body has n-fold rotation axis (represented as 'n'), a rotation of $360^{o}/n$ about that axis will bring it into coincidence with itself. A lattice can possess more than one symmetry element. Point groups define the symmetry elements possessed by a lattice. There are 32 point groups.

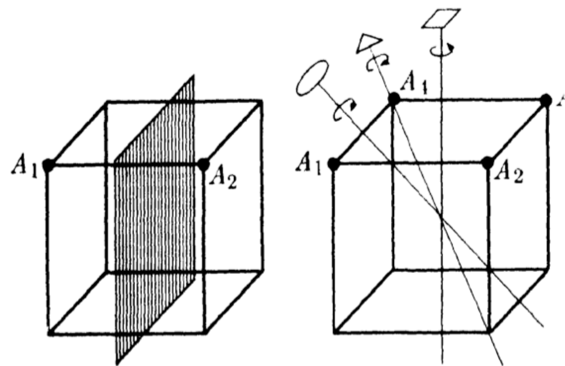

Figure 2.3: Operation of symmetry elements mirror plane and rotation axes [10].

Until now, lattices were discussed instead of actual crystals. Discussion on actual crsytals should start with stating the relation between lattice points in a Bravais lattice and atoms (or ions or molecules) of a crystal. For each lattice point, there is one or more atom in the crystal related to it. Hence actual crystals possess the symmetry elements of their Bravais lattice.

It is possible to have one atom on one lattice site which is simple to imagine. Copper, for example, has face-centered cubic structure. Each copper atom sits onto a lattice point. There are also crystals in which more than one

atom is related to one lattice point. Zinc, for example, has a hexagonal closed packed (HCP) structure. There are two atoms per unit cell. (Figure 2.4(a)). HCP structure belongs to hexagonal Bravais lattice. Each lattice point is related to two Zn atoms (Figure 2.4(b)). Atoms shown in Figure 2.4(a) are marked with x in Figure 2.4(b).

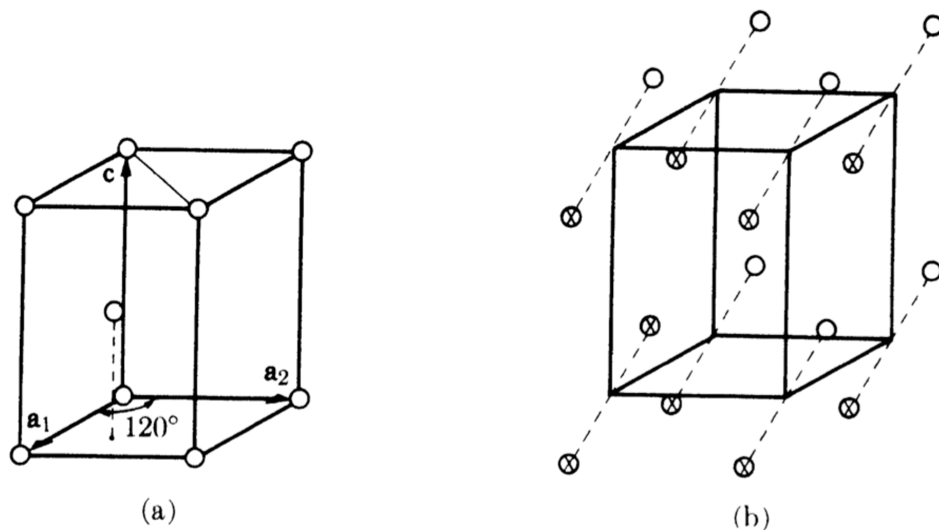

Figure 2.4: (a) Atomic arrangement of a hexagonal close packed structure, circles represent atoms (b) Hexagonal lattice with two atoms per lattice point. Atoms marked with x are atoms shown in (a) [10].

There are also compounds to consider. They have more than one type of atom therefore additional rules are applied. First, same kind of atoms form a crystal structure. For example, structure shown in Figure 2.5(a) is simple cubic not body centered cubic. Secondly, atoms of same kind should possess the same symmetry, independent of each other, with the entire crystal (Figure 2.5(b)).

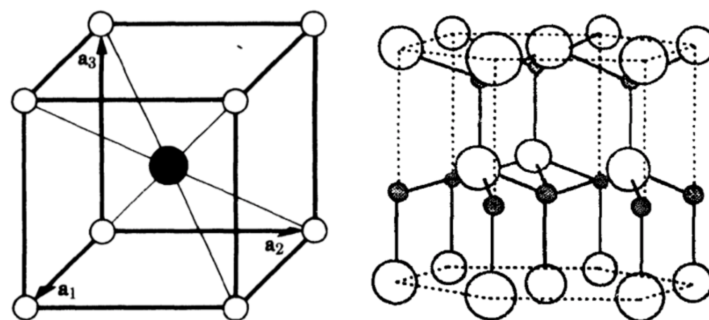

Figure 2.5: Crystal structure of CsCl(a) [10], ZnO(b) [11].

2.1.3 Tensors

Piezoelectricity is not a scalar quantity, it is direction dependent. Therefore tensors should be used to define piezoelectric effect. Tensors are multi-dimensional array of numbers. It is different from a matrix in the sense that a tensor has a physical meaning, it describes a physical quantity. It can be said that tensor is a matrix with attitude. Rank of a tensor can be defined as the number of directions needed to define a tensor. The number of indices of a tensor coefficient is also equal to the rank of the tensor. Scalar quantities like temperature and density are tensors of zero-rank. Vectors are tensors of first-rank.

Coefficients of a tensor are determined according to the choice of axes. If axes change, coefficients would also change. However, both tensors would represent the same physical quantity. For the reasons revealed later in this chapter, it is important to understand how transformations should be performed, therefore it will be worked out with examples.

As a first example, it will be shown how a first rank tensor, a vector, components transform when the axes are transformed. Consider x_1, x_2, x_3 axes were transformed into new set of axes x_1', x_2', x_3'.

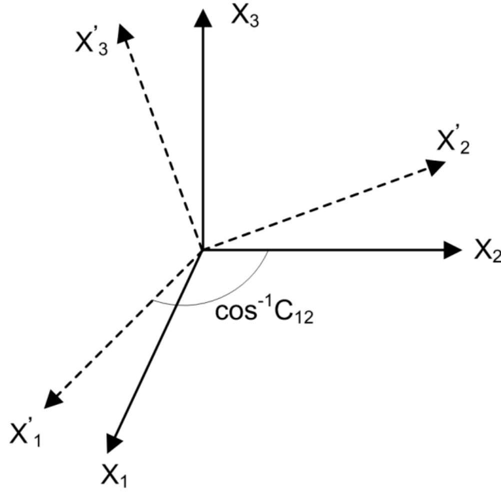

Figure 2.6: Transformation of axes. Angle between $x_1^'$ and x_2 is shown.

C_{ij} is the cosine of the angle between $x_i^'$ and x_j. It is called a direction cosine and the array of C_{ij} values are represented by the matrix $\left(C_{ij}\right)$. Direction cosines of $x_1^'$ with respect to x_1, x_2, x_3 are C_{11}, C_{12}, C_{13}.

$$C_{ij} = \begin{pmatrix} C_{11} & C_{12} & C_{13} \\ C_{21} & C_{22} & C_{23} \\ C_{31} & C_{32} & C_{33} \end{pmatrix}$$

Suppose a vector **e** with components e_1, e_2, e_3. Component of **e** on new axes would be $e_1^', e_2^', e_3^'$. $e_1^'$ will be determined by the projection of components e_1, e_2, e_3 on it. Hence:

$$e_1^' = C_{11}e_1 + C_{12}e_2 + C_{13}e_3$$

Similarly,

$$e_2^' = C_{21}e_1 + C_{22}e_2 + C_{23}e_3$$

$$e_3^' = C_{31}e_1 + C_{32}e_2 + C_{33}e_3$$

In general form (using Einstein summation convention),

$$e_i^' = C_{ij}e_j$$

This is the transformation law for a vector, a first-rank tensor. Reverse tranformation law, that is the transformation from the new axes back to the old axes, would be defined as:

$$e_i = C_{ji} e'_j$$

Now consider we have two vectors **a** and **b**. For the set of axes x_1, x_2, x_3, they are related to each other with the second rank tensor T_{ij}, with the equation $\mathbf{a} = T_{ij}\mathbf{b}$ (e.g. the relation between electric field (E-field) which is a vector and current which is also a vector, is defined as conductivity which is a second rank tensor). If we define new set of axes x'_1, x'_2, x'_3, components of the vectors will change from a_i, b_i to a'_i, b'_i. We now wonder T'_{ij}, the relation between a'_i and b'_i, in terms of T_{ij}. This can be derived by writing a' in terms of a, a in terms of b, and b in terms of b'.

$$a'_i = C_{ij} a_j$$

$$a_j = T_{jk} b_k$$

$$b_k = C_{lk} b'_l$$

Combining to reach the relation between a'_i and b'_i,

$$a'_i = C_{ij} a_j = C_{ij} T_{jk} b_k = C_{ij} T_{jk} C_{lk} b'_l$$

$$a_i = T_{il}\, b_l$$

Then transformed tensor would be,

$$T'_{il} = C_{ij} T_{jk} C_{lk}$$

or more clearly,

$$T'_{AB} = C_{Aa} C_{Bb} T_{ab}$$

is the transformation law for the second-rank tensor. Reverse transformation would be given by

$$T_{AB} = C_{aA} C_{bB} T'_{ab}.$$

Piezoelectricity is a third rank tensor, therefore transformation law for a third rank tensor will be shown as a last derivation. For a third rank tensor, description of the relation between a vector P and a second rank tensor σ is,

$$P_i = d_{ijk}\sigma_{jk}$$

Transformation law for the third rank tensor, d_{ijk}, can be derived with similar arguments used to reach the law for the second rank tensor:

$$P_i^{'} = C_{ij}P_j$$

$$P_j = d_{jkl}\sigma_{kl}$$

$$\sigma_{kl} = C_{xk}C_{yl}\sigma_{xy}^{'}$$

Combining to reach the relation between $P_i^{'}$ and $\sigma_{xy}^{'}$,

$$P_i^{'} = C_{ij}P_j = C_{ij}d_{jkl}\sigma_{kl} = C_{ij}d_{jkl}C_{xk}C_{yl}\sigma_{xy}^{'}$$

$$P_i^{'} = d_{ixy}^{'}\sigma_{xy}^{'}$$

Transformation law for the third-rank tensor is,

$$d_{ixy}^{'} = C_{ij}C_{xk}C_{yl}d_{jkl}$$

2.1.4 Piezoelectricity

When a stress is applied to a crystal, electric moment occurs and under an electric field, a crystal strains. These two effects are called piezoelectricity, former being the direct one and the latter being the reverse one. Figure 2.7 simply shows how mechanical forces could unbalance dipole moments, resulting in polarization.

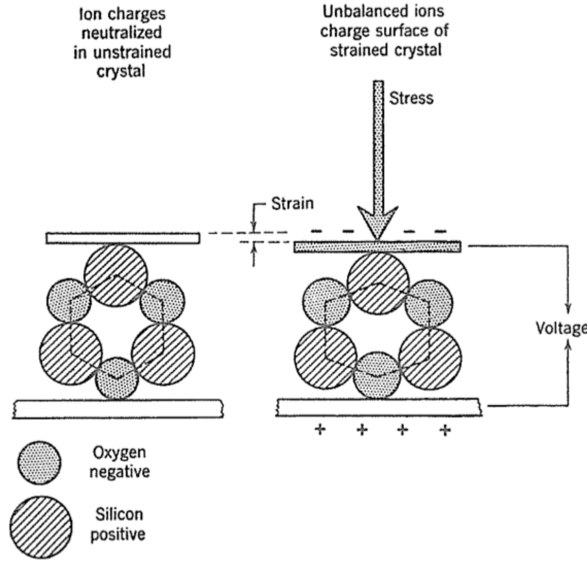

Figure 2.7: Ion positions in a quartz lattice with and without external stress [12].

Quartz is the one of the most widely known piezoelectric material. If a uniaxial stress (tensile or compressive) is applied along one of the 2-fold rotation axis of the quartz crystal, an electric moment will develop on the same axis.

$$P = d\sigma$$

P is the dipole moment and σ is the stress. Linear relation between them, d, is called piezoelectric modulus. Polarization changes direction according to the direction of stress (tensile or compressive). Stress is a second-rank tensor and polarization is a vector. 27 coefficients are needed to define the relation between them. Hence, piezoelectric moduli d_{ijk} is a third-rank tensor with 27 coefficients,

$$d_{ijk} = \begin{bmatrix} d_{111} & d_{112} & d_{113} & d_{121} & d_{122} & d_{123} & d_{131} & d_{132} & d_{133} \\ d_{211} & d_{212} & d_{213} & d_{221} & d_{222} & d_{223} & d_{231} & d_{232} & d_{233} \\ d_{311} & d_{312} & d_{313} & d_{321} & d_{322} & d_{323} & d_{331} & d_{332} & d_{333} \end{bmatrix}$$

P_1 can be written as,

$$P_1 = d_{111}\sigma_{11} + d_{112}\sigma_{12} + d_{113}\sigma_{13} + d_{121}\sigma_{21} + d_{122}\sigma_{22} + d_{123}\sigma_{23} + d_{131}\sigma_{31} + d_{132}\sigma_{32} + d_{133}\sigma_{33}$$

In general form (using Einstein notation),

$$P_i = d_{ijk}\sigma_{jk}$$

The piezoelectric moduli are equal for the direct and converse piezoelectric effects therefore if direct effect is formulated as $P_i = d_{ijk}\sigma_{jk}$, converse effect can be written as,

$$\varepsilon_{jk} = d_{ijk}E_i$$

where E-field, E_i, applied to a crystal produces strain, ε_{jk}, in the crystal. The piezoelectric moduli in direct and converse effects being equal are predicted by Lippmann and proved experimentally by Curie brothers.

There are piezoelectric constants other than *d*, such as *e*, *g*, and *h*. To calculate the E-field due to applied stress, one should first calculate polarization ($P = d\sigma$) then E-field can be calculated using ($E = P/\varepsilon_r$) where ε_r is relative permittivity. To define indirect relation such as this, *e*, *g*, and *h* are used.

$$P = d\sigma = \varepsilon_r E,$$

$$E = \frac{d}{\varepsilon_r}\sigma = g\sigma ,$$

$$g = \frac{d}{\varepsilon_r}$$

For the relation between strain and polarization, e,

$$P = d\sigma = dY\varepsilon = e\varepsilon,$$

$$e = dY$$

where Y is Young's Modulus. Last coefficient, h, defines the relation between E-field and strain,

$$P = d\sigma = dY\varepsilon = \varepsilon_r E$$

$$E = \frac{dY}{\varepsilon_r}\varepsilon$$

$$h = \frac{dY}{\varepsilon_r} = gE$$

There is one last important property left to define piezoelectricity thoroughly. That is electromechanical coupling coefficient, k^2. It defines the efficiency of transduction. If $k^2 = 0.2$, for example, this means 20% of the electric energy applied will be available as mechanical energy, and vice versa. Electromechanical coupling coefficient is related to piezoelectric constants as [12],

$$k^2 = ge$$

Elements of symmetry in a crystal reduce the number of independent variables in the piezoelectric moduli. If axes are transformed by one of the symmetry element present in the crystal, d_{ijk} should remain the same because crystal would be the same after the transformation. It is stated in the postulate known as Neumann's Principle.

'The symmetry elements of any physical property of a crystal must include the symmetry elements of the point group of the crystal'.

Among 32 crystal classes, 20 of them exhibit piezoelectricity. These are the non-centrosymmetric point groups except 432.

Piezoelectric crsytal classes are: 1, 2, m, 222, mm2, 4, 4, 422, 4mm, 42m, 3, 32, 3m, 6, 6, 622, 6mm, 62m, 23, 43m.

To illustrate the effect of symmetry on the piezoelectricity, piezoelectric moduli for the 6mm point group will be derived in the next section. It is the point group possessed by ZnO.

2.1.5 Derivation of the piezoelectric moduli for the point group 6mm

Piezoelectric moduli will be transformed with the application of each symmetry element. The moduli after transformation should be equal to the moduli before transformation due to Neumann's principle. Figure 2.8 shows the symmetry elements of the point group 6mm. Although there are six mirror planes, only two of them are distinct. Consider one of the planes shown by the dotted line, with the application of 6-fold rotation axis on that plane other two planes shown with the dotted lines can be obtained therefore they are not distinct. Two distinct planes are shown by dotted and straight lines.

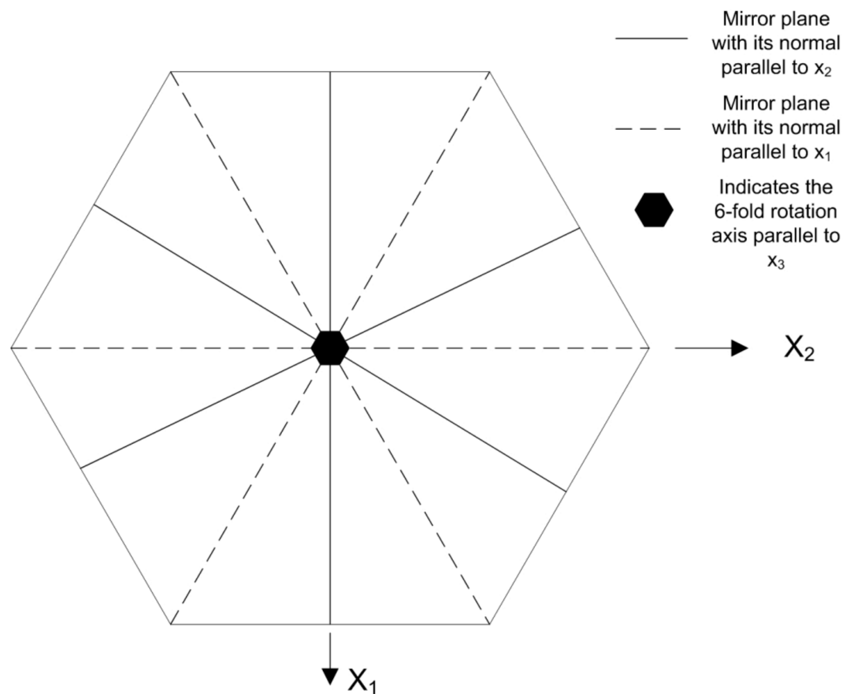

Figure 2.8: Symmetry elements of the point group 6mm. A six-fold rotation axis, two mirror planes. x_1 and x_2 axes are shown. x_3 axis is parallel to the 6-fold rotation axis, with the direction out of the page.

Firstly, restrictions imposed by the mirror plane whose normal is parallel to x_2 will be examined (shown by the straight line in Fig. 2.8). Figure 2.9 shows how this mirror plane transforms the axes.

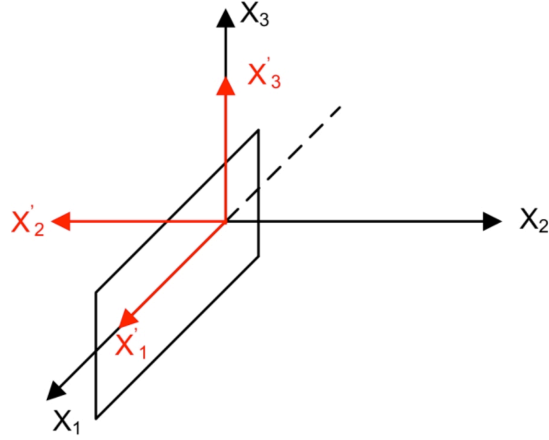

Figure 2.9: Transformation of axes by the mirror plane shown by the straight line.

Now direction cosines for this transformation should be determined, remembering C_{ij} is the cosine of the angle between $x_i^{'}$ and x_j. For example C_{22} is the cosine of the angle between $x_2^{'}$ and x_2, which is $\cos(\pi) = -1$. Whole matrix should be,

$$C_{ij} = \begin{pmatrix} 1 & 0 & 0 \\ 0 & -1 & 0 \\ 0 & 0 & 1 \end{pmatrix}$$

Only non-zero direction cosines are $C_{11} = 1,\ C_{22} = -1, C_{33} = 1$. Transformation law for the third-rank tensor is,

$$d_{ijk}^{'} = C_{iI} C_{jJ} C_{kK} d_{IJK}$$

Coefficients of the moduli $d_{ijk}^{'}$ should be equal to d_{IJK} after this transformation. Let us start with considering first coefficient,

$$d_{111}^{'} = C_{1I} C_{1J} C_{1K} d_{IJK}$$

$$d_{111}^{'} = C_{11}C_{11}C_{11}d_{111} + C_{11}C_{11}C_{12}d_{112} + C_{11}C_{11}C_{13}d_{113} + C_{11}C_{12}C_{11}d_{121} + \ldots$$

All components following the first component $C_{11}C_{11}C_{11}d_{111}$ contain C_{12} or C_{13} which is zero. Therefore $C_{11}C_{11}C_{11}d_{111}$ is the only non-zero component, $d_{111}^{'}$ becomes,

$$d'_{111} = C_{11}C_{11}C_{11}d_{111} + 0 + 0 + 0... = C_{11}C_{11}C_{11}d_{111} = d_{111}$$

$d'_{111} = d_{111}$ this means d_{111} can take any value, there is no restriction imposed by the mirror plane (Fig. 2.9) on the value of this coefficient. Consider the second coefficient,

$$d'_{112} = C_{1I}C_{1J}C_{2K}d_{IJK}$$

$$d'_{112} = C_{11}C_{11}C_{21}d_{111} + C_{11}C_{11}C_{22}d_{112} + C_{11}C_{11}C_{23}d_{113} + ...$$

Implementing the same approach used in d'_{111} . The only non-zero term is $C_{11}C_{11}C_{22}d_{112}$ hence,

$$d_{112} = 0 + C_{11}C_{11}C_{22}d_{112} + 0 + 0 + ... = C_{11}C_{11}C_{22}d_{112} = -d_{112}$$

$$d'_{112} = -d_{112}$$

then, d'_{112} and d_{112} must be equal to zero in order to satisfy both Neumann's principle ($d'_{112} = d_{112}$) and the restriction ($d'_{112} = -d_{112}$) imposed by the transformation according to the mirror plane in Figure 2.9.

$$d'_{112} = -d_{112} = 0$$

There are 27 components, it would be tiresome to do this calculation for each of them. This derivation can be performed more easily. It should be realized that $C_{xy} = 0$ and $C_{xx} = 1,-1$ for the direction cosine of the transformation due to mirror plane in Figure 2.9.

Consider again, the transformation law $d'_{ijk} = C_{iI}C_{jJ}C_{kK}d_{IJK}$. If $i \neq 2, j \neq 2, k \neq 2$ then direction cosines will be either one or zero. Examine the case for the $d'_{111} = C_{1I}C_{1J}C_{1K}d_{IJK}$. Therefore $d'_{ijk} = d_{ijk}$ and there will be no restriction for the coefficients with the indices $i \neq 2, j \neq 2, k \neq 2$. If only one of the i, j, k is 2 then $d'_{ijk} = -d_{ijk}$. d_{ijk} is zero for coefficients with only one indice is equal to 2. Examine the case for the $d'_{112} = C_{1I}C_{1J}C_{2K}d_{IJK}$ above. If two of the indices i, j, k are equal to 2 than $d'_{ijk} = d_{ijk}$ (since $(-1)\times(-1) = 1$). There is no restriction. If, finally, $i = j = k = 2$ than $d'_{ijk} = -d_{ijk}$. Therefore $d_{ijk} = 0$.

Now restrictions imposed by the mirror plane could be tabulated in order to understand the result more clearly (Table 2.1).

Table 2.1: Restrictions imposed on d_{ijk} by the mirror plane whose normal is parallel to x_2

i \ jk	11	12	13	21	22	23	31	32	33
1		0		0		0		0	
2	0		0		0		0		0
3		0		0		0		0	

Now let us consider the restrictions imposed by the other mirror plane (Figure 2.10).

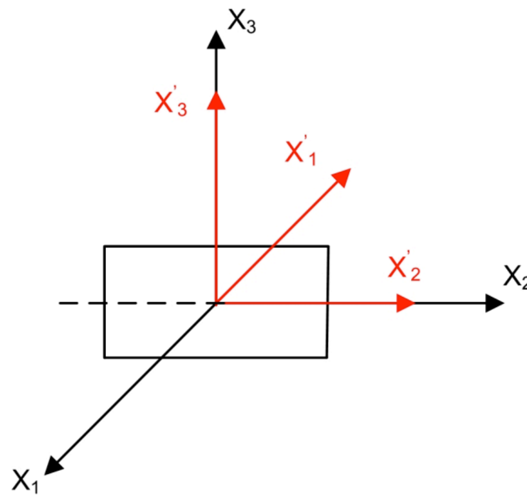

Figure 2.10: Transformation of axes by the second mirror plane.

For this transformation of axes, direction cosine matrix would be,

$$C_{ij} = \begin{pmatrix} -1 & 0 & 0 \\ 0 & 1 & 0 \\ 0 & 0 & 1 \end{pmatrix}$$

Using the similar arguments used to derive the restrictions imposed by the mirror plane in Figure 2.9, restrictions for the mirror plane in Figure 2.10 can be listed as follows,

Table 2.2: Restrictions imposed on piezoelectric moduli coefficients.

$i \neq 1, j \neq 1, k \neq 1$	$d'_{ijk} = d_{ijk}$	No restriction
One indice equal to 1	$d'_{ijk} = -d_{ijk}$	$d_{ijk} = 0$
Two indices equal to 1	$d'_{ijk} = d_{ijk}$	No restriction
$i = j = k = 1$	$d'_{ijk} = -d_{ijk}$	$d_{ijk} = 0$

The result of the restrictions can be tabulated as follows (Table 2.3),

Table 2.3: Resulting d_{ijk} after the restrictions in Table 2.2 are applied.

i \ jk	11	12	13	21	22	23	31	32	33
1	0				0	0		0	0
2		0	0	0			0		
3		0	0	0			0		

Combining both restrictions would yield (Table 2.4),

Table 2.4: d_{ijk} after the restrictions imposed by both mirror planes.

i \ jk	11	12	13	21	22	23	31	32	33
1	0	0	d_{113}	0	0	0	d_{131}	0	0
2	0	0	0	0	0	d_{223}	0	d_{232}	0
3	d_{311}	0	0	0	d_{322}	0	0	0	d_{333}

Here, it should be noted that d_{113} and d_{131} are equal because the stess tensor is symmetric ($\sigma_{jk} = \sigma_{kj}$). In general $d_{ijk} = d_{ikj}$, and there is one symmetry operation left to study and five independent coefficients, d_{113}, d_{223}, d_{311}, d_{322} and d_{333}.

Figure 2.11 shows the transformation of axes with the application of 6-fold rotation axis ($360^o/6 = 60^o$ rotation), parallel to x_3.

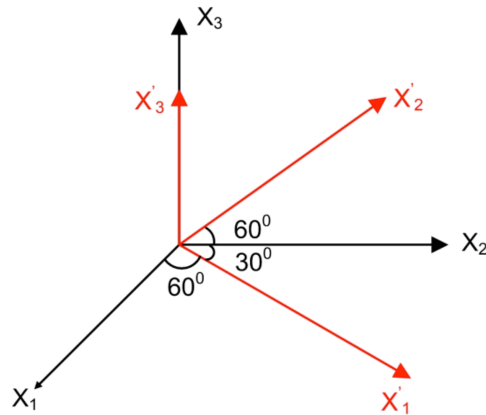

Figure 2.11: Transformation of axes due to 6-fold rotation axis.

For this transformation, direction cosines are given as,

$$C_{ij} = \begin{pmatrix} 0.5 & \sqrt{3}/2 & 0 \\ -\sqrt{3}/2 & 0.5 & 0 \\ 0 & 0 & 1 \end{pmatrix}$$

For the first component d_{113},

$$d'_{113} = C_{1I}C_{1J}C_{3K}d_{IJK}$$

Since C_{3K} is non-zero only when K=3,

$$d'_{113} = C_{1I}C_{1J}C_{3K}d_{IJK} = C_{1I}C_{1J}C_{33}d_{IJ3} = C_{1I}C_{1J}d_{IJ3}$$

$$d_{113} = C_{11}C_{11}d_{113} + C_{11}C_{12}d_{123} + C_{12}C_{11}d_{213} + C_{12}C_{12}d_{223}$$

Since d_{123} and d_{213} are zero,

$$d'_{113} = C_{11}C_{11}d_{113} + C_{12}C_{12}d_{223} = 0.5^2 d_{113} + (\sqrt{3}/2)^2 d_{223} = 0.25 d_{113} + 0.75 d_{223}$$

Solving together with the equation $d'_{113} = d_{113}$,

$$d_{113} = d_{223}$$

For the d'_{311},

$$d'_{311} = C_{3I}C_{1J}C_{1K}d_{IJK} = C_{1J}C_{1K}d_{3JK}$$

$$d'_{311} = C_{11}C_{11}d_{311} + C_{11}C_{12}d_{312} + C_{12}C_{11}d_{321} + C_{12}C_{12}d_{322}$$

$$d'_{311} = 0.25 d_{311} + 0.75 d_{322}$$

$$d_{311} = d_{322}$$

For the last coefficient d_{333},

$$d'_{333} = C_{3I}C_{3J}C_{3K}d_{IJK}$$

Since C_{3x} is either zero or one,

$$d'_{333} = d_{333}$$

Combining all restrictions would give all coefficients for the 6mm point group (Table 2.5),

Table 2.5: Coefficients of the piezoelectric moduli after restrictions imposed by the transformations due to symmetry elements 6, m, m.

i \ jk	11	12	13	21	22	23	31	32	33
1	0	0	d_{113}	0	0	0	d_{113}	0	0
2	0	0	0	0	0	d_{113}	0	d_{113}	0
3	d_{311}	0	0	0	d_{311}	0	0	0	d_{333}

In conclusion, there are only three independent coefficients d_{113}, d_{311}, d_{333} in a piezoelectric moduli of a crystal belonging to the point group 6mm.

$$d_{ijk} = \begin{bmatrix} 0 & 0 & d_{113} & 0 & 0 & 0 & d_{113} & 0 & 0 \\ 0 & 0 & 0 & 0 & 0 & d_{113} & 0 & d_{113} & 0 \\ d_{311} & 0 & 0 & 0 & 0 & 0 & 0 & 0 & d_{333} \end{bmatrix}$$

There is a convention used to reduce the tensor. Stress tensor is a symmetric tensor (i.e $\sigma_{jk} = \sigma_{kj}$) therefore there are six independent components instead of nine. Reduced notation for the stress tensor is as follows,

$$\sigma_i = \begin{pmatrix} \sigma_1 & \sigma_6 & \sigma_5 \\ \sigma_6 & \sigma_2 & \sigma_4 \\ \sigma_5 & \sigma_4 & \sigma_3 \end{pmatrix}$$

For this reduction,

$$\begin{aligned} P_i &= d_{i1}\sigma_1 + d_{i2}\sigma_2 + d_{i3}\sigma_3 + d_{i4}\sigma_4 + d_{i4}\sigma_4 + d_{i5}\sigma_5 + d_{i5}\sigma_5 + d_{i6}\sigma_6 + d_{i6}\sigma_6 \\ &= d_{i1}\sigma_1 + d_{i2}\sigma_2 + d_{i3}\sigma_3 + 2d_{i4}\sigma_4 + 2d_{i5}\sigma_5 + 2d_{i6}\sigma_6 \end{aligned}$$

Here coefficient 2 creates a problem for representing this equation in general form. This can be overcomed as follows. Right now $d_{i23} = d_{i32} = d_{i4}$ and $d_{i23} + d_{i32} = 2d_{i4}$

By defining,

$$\begin{aligned} d_{i23} + d_{i32} &= d_{i4} \\ d_{i13} + d_{i31} &= d_{i5} \\ d_{i12} + d_{i21} &= d_{i6} \end{aligned}$$

$$P_i = d_{i1}\sigma_1 + d_{i2}\sigma_2 + d_{i3}\sigma_3 + d_{i4}\sigma_4 + d_{i5}\sigma_5 + d_{i6}\sigma_6$$

$$P_i = d_{ij}\sigma_j$$

According to this reduction, reduced piezoelectric module for the 6mm point group would be,

$$d_{ij} = \begin{bmatrix} 0 & 0 & 0 & 0 & d_{15} & 0 \\ 0 & 0 & 0 & d_{15} & 0 & 0 \\ d_{31} & d_{31} & d_{33} & 0 & 0 & 0 \end{bmatrix}$$

where,

$$d_{15} = d_{113} + d_{131} = 2d_{113}$$

$$d_{31} = d_{311}$$

$$d_{33} = d_{333}$$

2.1.5 Piezoelectricity of ZnO

ZnO is a wide-band gap semiconductor and has a variety of applications in today's technology. Possible crystal structures of ZnO are wurtzite, zinc blende and rocksalt. Wurtzite is the thermodynamically stable phase at ambient conditions. Zinc-blende ZnO can be grown on cubic substrates while the rocksalt structure could be grown in high pressures.

In the wurtzite structure, each Zn is surrounded by four O atoms where Zn atom resides in the middle of a tetrahedron and O atoms sit at the corners of the tetrahedron, and vice versa. This arrangement is typical of sp^3 covalent bonding but ZnO also possesses ionic character. Ionicity of ZnO is at the boundary between ionic and covalent semiconductor [13]. Without this ionic character ZnO would not exhibit piezoelectricity since ionicity is required to form electric moment.

There are wide variety of deposition techniques to deposit thin film ZnO. These include sputtering, sol-gel process, pulsed laser deposition, atomic layer deposition, molecular beam epitaxy, metal-organic vapor deposition, and plasma enhanced chemical vapor deposition [14]. ZnO thin film reported in this work is deposited using rf-magnetron sputtering. Sputtering is a simple technique, in which required orientation for piezoelectricity can be obtained at room temperature independent of the substrate used. (0001) plane, which is the basal plane of ZnO, has the lowest surface free energy (Figure 2.12). Therefore, sputtered ZnO has a (0001) preferred orientation. Basal planes are parallel to the surface of the film [11].

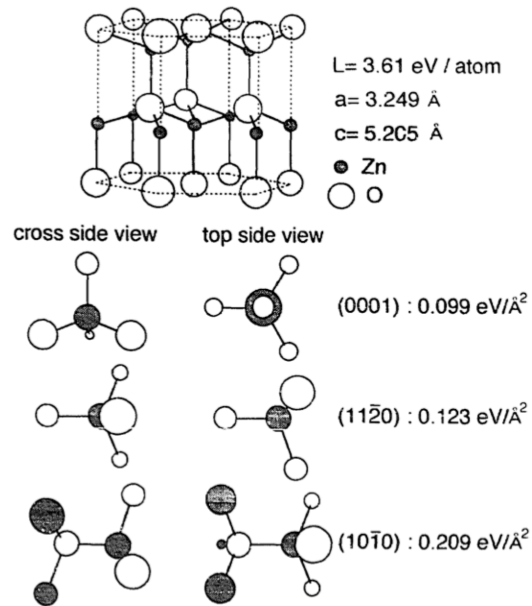

Figure 2.12: Crystal structure and surface free energies for three different planes of ZnO [11].

As demonstrated in section 2.1.5, piezoelectric moduli of ZnO has three independent coefficients d_{15}, d_{31}, d_{33}. These are [12],

$$d_{ij} = \begin{bmatrix} 0 & 0 & 0 & 0 & -12 & 0 \\ 0 & 0 & 0 & -12 & 0 & 0 \\ -4.7 & -4.7 & 12.0 & 0 & 0 & 0 \end{bmatrix} pC/N$$

Remembering the converse effect, $\varepsilon_{jk} = d_{ijk} E_i$ and $d_{15} = 2d_{113}$, $d_{31} = d_{311}$, $d_{33} = d_{333}$, it should be noted that only E-fields in the direction of [100] and [001] produce strain in the ZnO crystal.

2.2 Theory of SAW devices

2.2.1 Theory of Operation

Basic working principle behind the SAW devices is conversion of electromagnetic (EM) waves into acoustic waves and converting acoustic waves back into the electromagnetic waves. Interdigital transducers (IDTs) are used for both of the conversions. In the former conversion, reverse piezoelectric effect is utilized whereas latter conversion uses direct piezoelectric effect. As illustrated in Figure 2.13, when a potential difference is applied between the fingers of an IDT, E-field lines pass from the piezoelectric substrate.

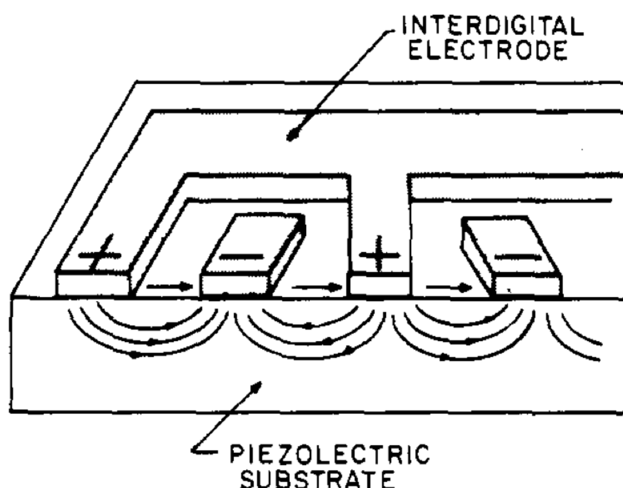

Figure 2.13: Interdigital transducer function on a piezoelectric material [15].

Since the material is piezoelectric, E-field causes mechanical deformation which is known as reverse piezoelectric effect, assuming that the material and its crystallographic orientation is convenient for this conversion (Section 2.1). If the applied E-field is oscillating, then resulting mechanical deformation will also be oscillating. Oscillating mechanical fields cause mechanical waves in the solid. They travel perpendicular to the long edges of the IDT finger in both directions. Mechanical waves deform the crystal as they travel and due to direct piezoelectric effect, there is a potential field accompanying the mechanical

wave. If this wave reaches another IDT, a potential difference will occur within the IDT finger pairs due to direct piezoelectric effect. This is how a SAW device basically works (Figure 2.14).

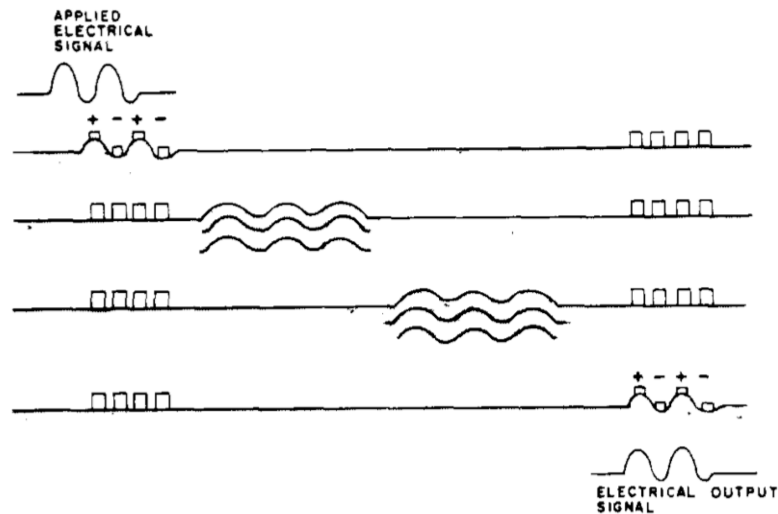

Figure 2.14: Basic working principle of a SAW device. Edge view [15].

There are two main configurations for SAW devices. First one is the SAW delay line and the other one is the SAW resonator. SAW delay line is the device described in Figure 2.14. Figure 2.15 illustrates top view of a SAW delay line. There are two IDTs at the same surface apart from each other with a propagation length of L. Input IDT converts EM signal to acoustic wave, it travels to the output IDT and converts back to an EM signal. It is called as a delay line because acoustic wave travels the distance L much slower than an EM signal. Therefore, the signal is delayed between two IDTs. In the second configuration, one or two IDTs are used to construct a resonant cavity. In this configuration, generated acoustic wave reflects back from the ends of the substrate and starts to resonate which can be detected using the generating IDT or another one. Devices fabricated in this work are SAW delay lines.

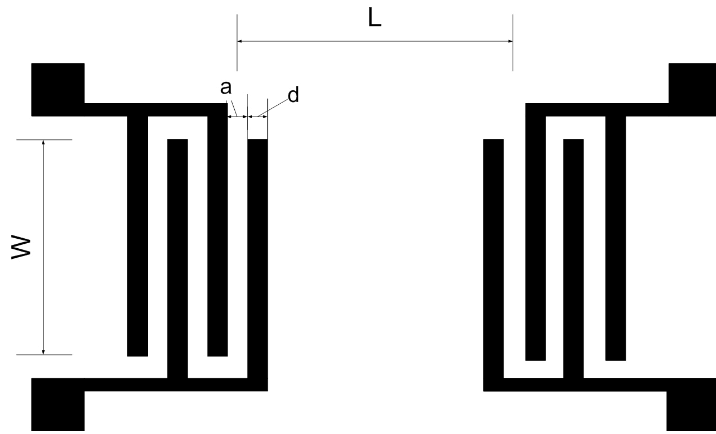

Figure 2.15: Surface acoustic wave delay line with interdigitated transducer dimensions.

IDT dimensions (Figure 2.15) determine the wavelength of the acoustic waves. Each IDT pair generates acoustic waves. When a generated wave in one pair meets with the other wave generated in the next finger pair, they interfere. If the distance between finger pair centers is an integer multiple of the wavelength of the wave, then constructive interference occurs, the other wavelengths destruct each other. Therefore, the SAW wavelength is defined as $\lambda = 2(a + d)$ and the central frequency is defined as,

$$f_0 = \frac{v_0}{\lambda}$$

where subscript 0 stands for the unperturbed values. v_0 is the acoustic wave velocity and it depends on the substrate material, orientation of the substrate and the type of the wave generated. When the propagation of the SAW is perturbed somehow, velocity of the wave changes. This perturbance can be measured as the frequency shift. Measurement of this perturbance is the principle behind SAW sensors.

Frequency of the acoustic waves ranges from few MHz to GHz. Sizes of the devices depend on the frequencies. Smaller devices are needed for higher frequencies (as d decreases, wavelength decreases which in turn increases the frequency). The limit for smaller devices is the fabrication technologies

available. For lower frequencies, devices should enlarge and this is limited by the substrate size.

Dimensions of the IDTs are given in Figure 2.15. L is the propagation length. Increasing L results in an increase in attenuation whereas a decrease in noise levels. Numbers of finger pairs, N, determine the frequencies around the central frequency, which is called as bandwidth (f_0/N). Increasing finger pairs decreases bandwidth because frequencies near the central frequency would survive if there is less finger pairs, as the finger pairs increase the constructive interference increases for the near-central frequencies. a is the finger spacing and d is the finger width. Metallization ratio is defined as the ratio of the area coated with metal to the electrode area, which is given by the formula $r = d/(d+a)$. In this work, metallization ratio is fixed to 0.5 (i.e. $d = a$). Final dimension, W, is the overlap of fingers which is termed as aperture.

It is important to note that, other than using a piezoelectric substrate (e.g. quartz, $LiNbO_3$) for the fabrication of SAW devices, a piezoelectric thin film (e.g. ZnO, AlN) over a non-piezoelectric substrate (e.g. Si) could be utilized. The advantage of using a piezoelectric thin film is its applicability to variety of substrates. Using Si as the substrate, SAW device can be implemented to electronic circuits. In this study, ZnO was used as the piezoelectric film and silicon was used as the substrate.

As explained before, E-field in the directions [100] and [001] are the only directions to produce strains in the ZnO wurtzite crystals and sputtered ZnO grows with its c-axis (i.e. [001] direction) perpendicular to the surface. IDTs parallel to the ZnO surface will create curved E-fields with components perpendicular and parallel to the surface (Figure 2.13). Perpendicular E-field components are in the [001] direction since c-axis is also perpendicular to the surface. Therefore this configuration leads to ZnO based SAW devices. Thus it can be deduced that improving c-axis orientation of ZnO will improve

piezoelectricity and this will improve the device performance by increasing the efficiency of transduction

2.2.2 Surface Waves

In this part, nature of the surface acoustic waves will be stated. There are three fundamental particle motions constituting wave motion. These are linear, circular and elliptical motions. Longitudinal (2.16(a)) waves and the transverse (2.16(b)) waves are the two basic wave types.

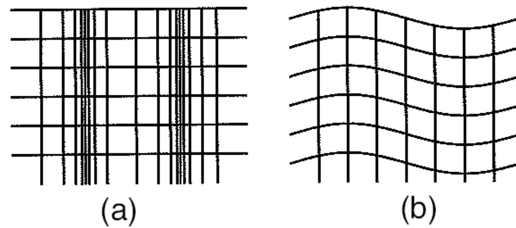

Figure 2.16: (a) Longitudinal, (b) Transverse wave [16].

In transverse (shear) waves, particle motion and wave propagation is perpendicular to each other whereas in longitudinal (compressional) waves, particle motion and the wave propagation are parallel. In a transverse wave, direction of the particle motion determines the polarization of the wave and propagation direction of the wave determines the energy transfer direction.

For shear waves propagation along a surface, there exist two important vibration types which are shear vertical and shear horizontal (Figure 2.17).

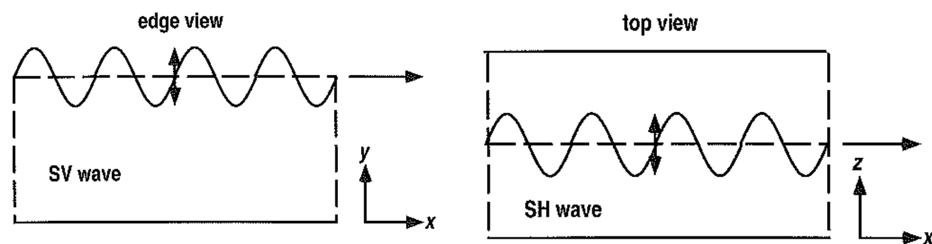

Figure 2.17: Shear vertical and shear horizontal vibration types [16].

Surface acoustic waves were first described by Lord Rayleigh in 1885 [17]. The particle motion in Rayleigh waves is elliptical. The wave has both compressional and shear components. Elliptic motion is in the plane perpendicular to the surface. Wave propagation is parallel to the elliptical motion and the surface plane. Major axis of the ellipse is perpendicular to the surface. Particle motion is counter-clockwise when the wave moves from left to right. Rayleigh waves attenuate exponentially going from surface to the bulk of the substrate, and its energy is confined to one wavelength of thickness.

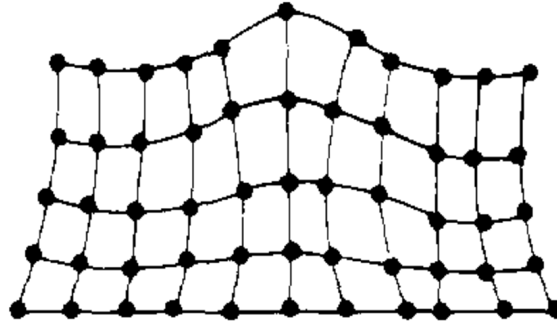

Figure 2.18: A schematic illustration of Rayleigh Wave [18].

Consider a Rayleigh wave with $\lambda = 20\mu m$ and a piezoelectric substrate with a thickness of $500\mu m$. Since Rayleigh wave travels in the top $20\mu m$, thickness of the substrate is not very important in this case. But in a layered structure such as ZnO-Si, ZnO thickness can vary from few hundreds of nanometers to few tens of microns therefore it affects wave propagation. For this case, normalized thickness (i.e. h/λ) should be considered. It can be defined as h/λ where h is the layer thickness and λ is the wavelength. Within the range $0.04 \le h/\lambda \le 0.15$ Rayleigh wave is the fundamental wave mode [14, 16, 19].

Above this range, a second order Rayleigh wave, called Sezawa wave, appears along with the Rayleigh wave. Below this range, other acoustic modes such as plate waves occur. The devices studied in this work are within the range $0.04 \le h/\lambda \le 0.15$, therefore the acoustic mode utilized in these devices is Rayleigh wave.

2.2.3 Parameters Affecting Wave Propagation

It is important to understand the phenomena perturbing wave motion in order to interpret the device response correctly.

Temperature has considerable effect on wave propagation mainly because many material properties (material constants) are temperature dependent. The amount of perturbation depends on the material and the crystal orientation it possesses. This dependency also led to temperature sensors based on SAW devices [20].

Pressure is another important factor affecting SAWs. SAWs produce waves in the gas when they are in contact with it mainly due to its shear horizontal component. This causes attenuation in the SAWs and it is more prominent as the pressure increases. Pressure sensors were shown by Scherr et al. [21]. Liquid loading is another type of pressure. Measurements in liquid (e.g. SAW biosensor) causes liquid loading on the surface. Rayleigh wave seriously attenuates in this case, therefore a device utilizing a wave mode without shear horizontal component should be used.

As stated in Section 2.2.1, there is a potential field following the propagation of SAW. This potential field could be perturbed by an E-field applied close to it. This in turn would affect the propagation of the SAW. In addition, presence of a conducting or semi-conducting film on top of the substrate surface would perturb the wave due to electrical properties of the film apart from the mass loading.

One last property to consider is the surface roughness. Surface defects cause scattering of the SAWs. This results in attenuation of the wave. Additionally, this scattering could result in acoustic mode conversion [16, 22].

2.2.4 Measurement

The measurement of these devices is mainly done through network analyzers. Attenuation and phase shifting of the SAWs can be deduced from the scattering parameter S_{21}, which is the ratio of input and transmitted power. Since this transfer is done by acoustic waves, it is a measure of its characteristics. There are also oscillator based measurements. In this method, SAW device is used as a frequency controlling element of an oscillator circuit. For the measurements of SAW devices fabricated in this work, network analyzer is used.

2.3 Literature Overview

First effective SAW device appeared in 1965 [23]. White and Voltmer introduced IDTs for direct generation and detection of SAWs. Before this discovery, generation and detection were done using mechanical coupling of a transducer to the device body which was ineffective. Abundant ideas followed this discovery. Frequency and time domain devices to augment signal processing ability of microwave systems were developed first. Today, SAW market is a large, where the global market value of SAW devices reached nearly $1.1 billion in 2011 and it is expected to reach $1.8 billion by 2016 [24]. The main application field of these devices is telecommunications where it is used as a bandpass filter in RF range (e.g. in mobile phones). Still, SAW devices have wide variety of applications from wine tasting to satellite systems (Table 2.6).

Table 2.6 SAW device application areas after Hickernell [25]

Application area	Examples
Telecommunications:	Cellular, personal communication systems and networks, cordless, mobile, pagers, wireless local loops, base stations, global satellite.
Data Communications:	Digital radio, wireless local area networks, handheld data terminals, global positioning systems.
Video Applications:	Television, cable television, video cassette recorders, high definition TV, direct broadcast satellite TV, interactive TV, cable modems, video games.
Automotive and Home:	Remote keyless entry, theft deterrent systems, alarms, remote meter readings, home appliances, audio equipment, identification tags.
Military & Space:	Electronic warfare, signal intelligence, battlefield communications, avionics, fuzing, orbital and deep space satellite systems, surveillance system, missiles.
Other Markets:	Sensors, test equipment, high frequency clocks, computers, commercial avionics.

SAW devices fabricated in this work are intended to be used in sensing applications. Therefore, review of the SAW literature will focus mainly on sensor applications. The first SAW sensor was developed by Wohltjen et al. in 1979 [26]. They showed that surface molecules affect the wave propagation. Interactions were measured by the changes in amplitude and phase shift. They found that amplitude response is proportional to the pressure of the gas in the environment, and showed that response is proportional to (molecular weight)$^{1/2}$. In 1980, Fertsch, White and Muller showed that detection of organic vapors using polyvinyl chloride films on the delay line surface is possible [27]. In 1981, Bryant, Lee and Vetelino compared bulk acoustic wave (BAW) and SAW sensors for SO_2 and found that SAW sensor is able to detect SO_2 less than 100 ppb, which means SAW device is an order of magnitude more sensitive than BAW sensor [28].

Some of the vapor recognition materials and target vapors pairs reported in the literature are polyepichlorohydrine-toluene [29], polyisobutylene-octane [30], palladium-hydrogen [31] and zinc oxide-ammonia [32]. In addition, spray-coated composite polyethylenimine (PEI) with SiO_2/Si nanoparticles was used for the sensing of ethanol, and laser-deposited PEI was used for the sensing of methanol [33].

Biosensor applications of SAW devices were developed later, mainly because biosensors are usually required to work in liquids and Rayleigh waves attenuate seriously under liquid loading as explained in Section 2.2. In order to overcome this problem, device configurations utilizing acoustic modes such as surface transverse waves [34], shear horizontal SAWs [35] and Love Waves [36] were used.

In order to convert a SAW device to a biosensor, a layer responsive to the specific analyte is deposited onto the delay line surface. When the layer engages to the analyte, mass of the layer will increase and this will be reflected as a change in the acoustic wave. Using this method SAW biosensors were demonstrated for the detection of DNA [37], bacteria [38] and protein [39].

Devices fabricated in this work, layered ZnO-SiO_2-Si SAW devices utilizing Rayleigh waves, are first described in 1982 [40] and worked out until now [41-45].

Chapter 3

Experimental Details

In this chapter, firstly, SAW device fabrication process is described including the explanation of microfabrication steps, equipments used and process parameters in detail. Subsequently, methods and equipments used for the characterization of material properties of ZnO and properties of the SAW device are introduced.

3.1 Device Fabrication

This section provides a detailed explanation of the microfabrication process flow leading to the fabrication of SAW devices. All of the microfabrication processes were performed at UNAM Cleanroom Facility (UCF), in class 100 and class 1000 lab spaces.

3.1.1 Substrate and Surface Preparation

500 μm thick Si (100) wafer pieces were used as the substrate for the SAW devices. Wafers were cut into pieces using a diamond scriber. Surface cleanliness of the Si wafer pieces is important for the repeatability of materials and device characteristics as well as for good film adhesion onto the substrate surface. To eliminate particles and organic impurities on the surface, a three-stage substrate cleaning procedure was performed. First, samples were sonicated in acetone ($(CH_3)_2CO$) for 10 min to remove organic contamination. Afterwards, samples were sonicated in isopropyl alcohol ($(CH_3)_2CHOH$) for 10 min. Samples were rinsed with deionized (DI) water and dried with nitrogen gun. The final step was to bake pieces at 120°C for 5 min on a hot plate in order to eliminate any possible adsorbed water vapor remainings. Coating should be performed as soon as possible after cooling the sample to room temperature to avoid re-adsorption of water vapor from the environment.

3.1.2 SiO_2 Deposition Using RF Magnetron Sputtering

VAKSIS NanoD – 4S Magnetron Sputtering system was used for the deposition of 50 nm-thick SiO_2 (Figure 3.1). Si sputtering target with a 99.9999% purity was used. Oxygen was used as the sputtering gas together with argon in order to obtain SiO_2. This type of sputtering in which target material and sputter gas react to form the desired film is called reactive sputtering. Substrate was rotated during the depositions for film uniformity. Prior to each film deposition experiment, in order to eliminate the surface layer (i.e., native oxide, contamination layer, etc.) of the air-exposed sputtering target, pre-sputtering (target cleaning) procedure was conducted for one minute. Target-to-substrate distance was fixed to 15 cm. Base pressure of the system was below 6 x 10^{-6} Torr and chamber pressure during deposition was adjusted to 10 mTorr. Flow rates of Ar and O_2 were 50 sccm and 10 sccm, respectively. RF power was set to

150 W. Depositions were carried out at room temperature. Rate of deposition for this recipe was found as 2.8 nm/min.

Figure 3.1: VAKSIS NanoD – 4S Magnetron Sputtering system which was used for SiO_2, ZnO, Ti and Au thin film depositions.

3.1.3 ZnO Deposition Using RF Magnetron Sputtering

VAKSIS Magnetron Sputtering system has four magnetrons which allow to deposit four different materials sequentially without opening the reactor chamber. Two of the magnetrons are suitable for the deposition of insulators and semiconductors because they are RF powered. ZnO target and Si target were mounted in the chamber at the same time. Therefore, after SiO_2 deposition, ZnO could be deposited without breaking the chamber vacuum. Substrate rotation was active and pre-sputtering was performed for one minute. Optimized recipe used for the ZnO depositions is given in Table 3.1. Optimization of the recipe parameters is discussed in section 4.1.1.

Table 3.1: Optimized Sputtering Parameters for ZnO Deposition.

RF power	150W
Ar flow	50 sccm
O_2 flow	10 sccm
Chamber Pressure	5 mtorr
Temperature	Room temperature

3.1.4 Post-deposition Annealing of ZnO

After the depositions of SiO_2 and ZnO films, samples were annealed for texture improvement. Figure 3.2 shows ATV-Unitherm (RTA SRO-704) rapid thermal annealing (RTA) system used for post-growth annealing studies. Annealing process started with N_2 purge for 2 min to obtain an inert atmosphere. Samples were then heated to desired temperatures with a rate of 10°C/sec. Seven different temperatures (400-1000°C with 100°C increments) were used in this study. Annealing was performed for 5 and 30 min. After annealing, samples were cooled without any cooling source. Annealing chamber was opened when temperature reached below 100°C in order prevent unwanted surface reactions.

Figure 3.2: ATV-Unitherm (RTA SRO-704) rapid thermal annealing (RTA) system.

3.1.5 Formation of Interdigitated Transducers (IDT)

IDTs were fabricated with a three-stage microfabrication process. At the first stage, photoresist was patterned with photolithography. Then, a two-step titanium/gold (Ti/Au) sputtering process was performed with titanium as an adhesive layer. IDT formation is completed with a standard lift-off process.

3.1.5.1 Photolithography

After annealing the sample, surface preparation steps described in section 3.1.1 were repeated. Hexametyldisilazane (HMDS) is spin-coated before photoresist (PR) spinning to enhance the adhesion of the photoresist film. AZ5214E photoresist from AZ Electronic Materials was spin-coated (Figure 3.3(a)) which is a positive photoresist (PR) but is capable of behaving as a negative photoresist as well with the so-called "image reversal" process. Last two digits in the resist name (AZ52<u>14</u>E) indicate the film thickness attained by spin coating at 4000 rpm in 100 nm units (i.e. 1.4 μm for AZ5214E). In this study, both photoresist and HMDS were spinned at 4000 rpm for 40 seconds. Spinners should be as clean as possible before spinning because any residual particles on the spinner unit wall may contaminate the surface of the sample due to air flow formed during spinning. Substrates used for spin coating should be as rotation-symmetric as possible to prevent pronounced edge beads. Therefore, we preferred square-shaped symmetric samples instead of rectangle shaped ones.

After spin-coating, samples were baked in order to eliminate the remaining solvent in the film which is termed as soft-bake (Figure 3.3(b)). There are several reasons for reducing the solvent concentration in photoresist. Firstly, it is done to avoid mask contamination and sticking to the mask during contact mode lithography. Also soft-bake prevents bubbling during consecutive thermal processes. Finally, it enhances the photoresist adhesion to the substrate/film surface.

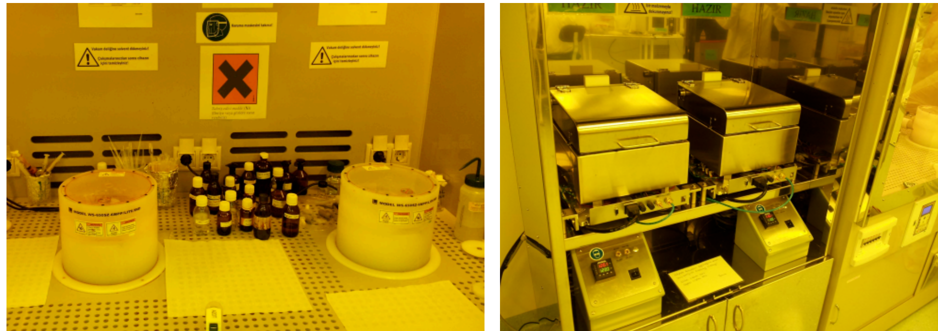

Figure 3.3: (a) Spinning of HMDS and AZ5214E were done in Laurell spinner system. (b) Precision hot plates where soft and hard-bake steps were performed.

Soft-bake was performed on a hot plate instead of an oven mainly because heat transfer mechanism in the oven is convection instead of conduction as in the case for a hotplate. Heating by convection causes different effective temperatures in the photoresist for first few minutes which is a problem for short baking steps like soft-baking. Therefore, samples were soft-baked on a hot plate at 110°C for 50 seconds.

Next step was the patterned exposure of the photoresist for the lift-off process. The lithography pattern is defined by a photomask which has the target pattern written on its Cr-coating. L-Edit software was used for the photomask CAD design. Photomask blanks were delivered as photoresist/chrome/glass from the mask manufacturer (Telic Inc.). These mask blanks were selectively exposed using Heidelberg Instruments DWL-66 Laser Mask Writer with a 4 mm write head (Figure 3.4). Masks became ready to use in lithography process after photoresist development, Cr etching in Cr-etchant solution and photoresist removal and mask cleaning process.

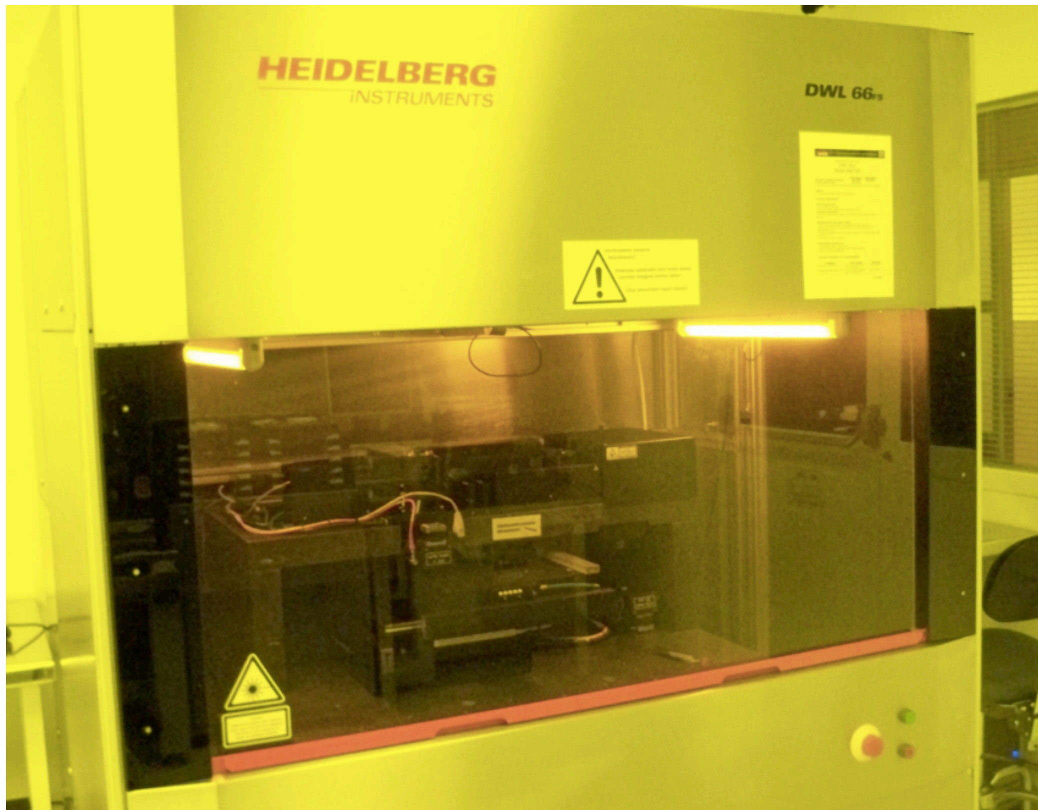

Figure 3.4: Heidelberg Instruments DWL-66 laser mask writer used for photomask production.

For the exposure step, Electronic Vision Group EVG 620 mask aligner was used (Figure 3.5). It has a Hg lamp equipped with i-line filter, which produces a collimated UV light-beam with a output wavelength of 365 nm. Exposure was performed with a dose of 40 mJ using soft contact mode. Photoactive compound in the photoresist (DNQ-sulfonate) is converted into indene carboxylic acid upon exposure by exchanging N_2 with H_2O and attaining several orders of magnitude higher alkaline solubility (development rate).

Figure 3.5: EVG 620 mask aligner used for the exposure of photoresist-coated wafers.

Development was carried out in AZ400K developer solution (AZ400K:H_2O = 1:5) for 1 min. Dissolved resist decreases the development rate of the developer. Therefore, it should be renewed after a maximum of two subsequent development processes.

The last step for photolithography is hard-bake. The intention for hardbake is to improve the stability of the photoresist for succeeding processes. Samples were baked at 120°C for 2 min on the hot plate.

3.1.5.2 Deposition of Titanium and Gold

Gold was selected as the IDT material due to its resistance to chemical reactions. VAKSIS NanoD – 4S Magnetron Sputtering system was used for depositing both materials. Titanium is used in order to enhance gold adhesion. Titanium and gold targets with a purity of 99.9999% were placed in the chamber at the same time. Base pressure of 6 x 10^{-6} Torr was reached before deposition. 3 nm-

thick titanium and 100 nm-thick gold were sputtered consecutively with the recipes given in Table 3.2.

Table 3.2: Sputtering parameters for titanium and gold.

	Titanium	Gold
DC power	125 W	75 W
Ar flow	8 sccm	50 sccm
Chamber pressure	10 mtorr	10 mtorr
Time	3 min	4 min

3.1.5.3 Lift-off

Lift-off is the final step for the fabrication process of the IDTs. Samples were placed in acetone and sonicated for 5 min. In order to prevent sticking of lifted-off metal back to the sample surface, samples were taken out of the acetone while sonication continues. Samples were quickly rinsed afterwards with iso-propyl alcohol and subsequently in DI water and dried with N_2 gun. If the inspection with optical microscopy reveals any metal sticking back again to the surface, sample was sonicated for one more minute in acetone. This sonication continued until the successful lifting-off of all unwanted metal parts. The applied microfabrication process flow is summarized in Figure 3.6 and Figure 3.7 shows optical micrographs of a successfully completed SAW device.

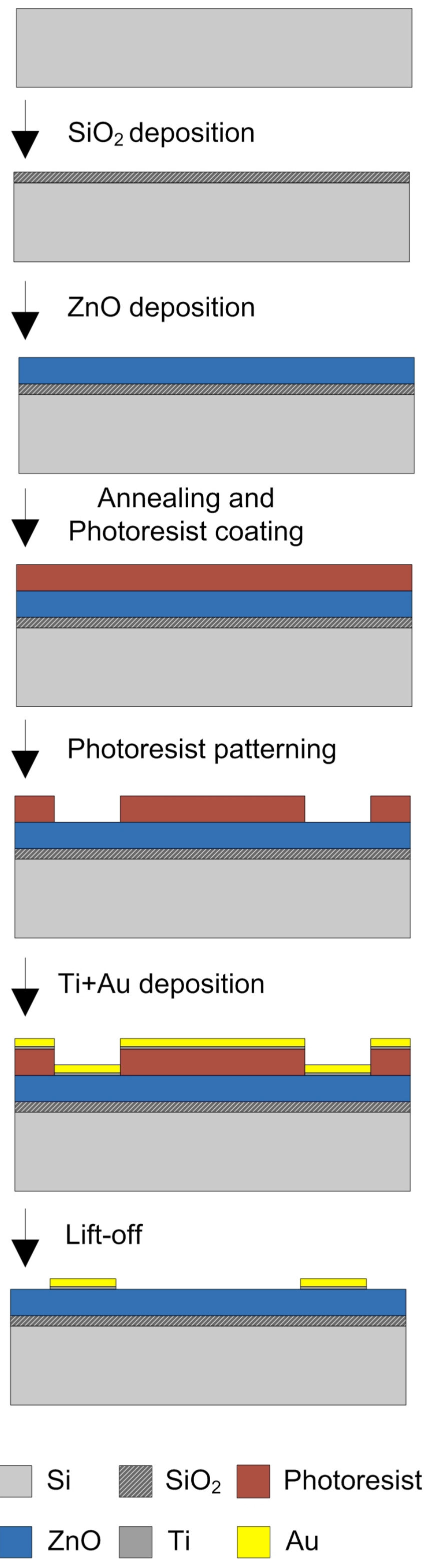

Figure 3.6: Microfabrication steps of SAW devices used in this work.

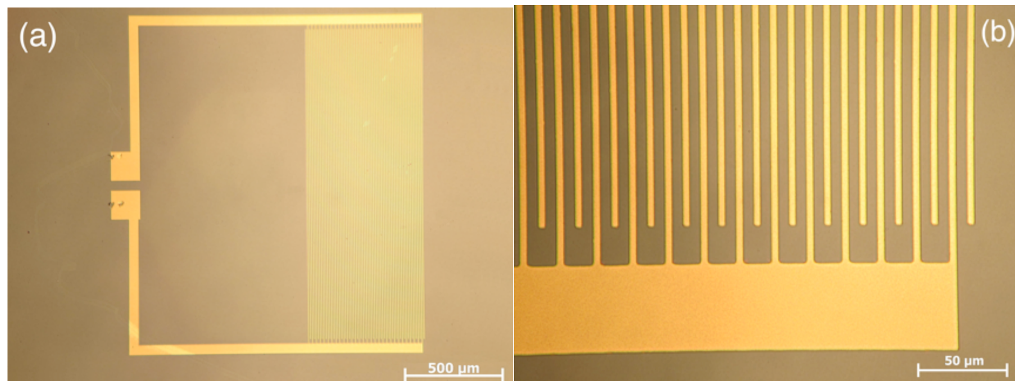

Figure 3.7: Optical microscope images of the final device showing gold electrodes over ZnO. (a) One of the interdigital transducers. (b) Finger pairs.

3.2 Characterization Methods

In this section, the methods used to characterize both ZnO thin film and fabricated SAW devices were described. ZnO films were characterized in terms of their structural, morphological, chemical and optical properties. Then, equipment used for the measurement of frequency dependence of insertion loss was explained.

3.2.1 Methods Used for ZnO Characterization

3.2.1.1 X-Ray Diffraction

X-ray diffraction (XRD) results from scattering of incident X-rays by the electrons of the host material atoms. Diffracted beam occurs only if some specific geometric conditions are satisfied. Since random arrangement of atoms (amorphous materials) would prevent any kind of geometric condition, some degree of crystallinity is required for an observable diffraction signal. Bragg's law could be used to state these specific geometric conditions:

$$n\lambda = 2d\sin\theta$$

Diffraction occurs when the angle between the incident beam and the surface, θ, satisfies the Bragg's law in which n is the order of diffraction, λ is the wavelength of the X-ray beam and d is the distance between the crystal planes. Bragg's law could be understood easily by examining Figure 3.8. $|KL|+|LM|$ is the path difference between the diffracted beams 1' and 2'. If this path difference is equal to whole number of wavelengths, then there will be no phase difference between the diffracted beams and constructive interference will occur which is called diffraction.

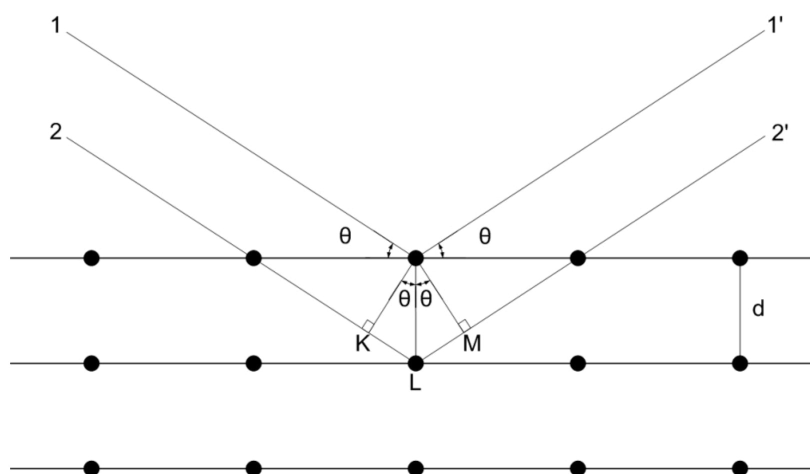

Figure 3.8: Schematic representation of Bragg's law.

Positions and the intensities of diffracted X-rays form the diffraction pattern of the material. This pattern is specific to the material under examination. Analysis of this pattern could reveal crucial structural information about the sample such as: crystal structure, lattice parameters, crystallite size, residual stress and phases present in the sample quantitatively.

XRD measurements of the ZnO films were performed in PANalytical X'Pert PRO Multi-Purpose X-Ray Diffractometer (Figure 3.9). Theta:Theta goniometer is used in this diffractometer. Target material of the tube is Cu hence the radiation used for diffraction is Cu Kα (λ=1.5418 Å). Tube voltage and tube

current were 45 kV and 40 mA, respectively. Scans were performed using 0.0066 step size and 0.0867 seconds count time per step.

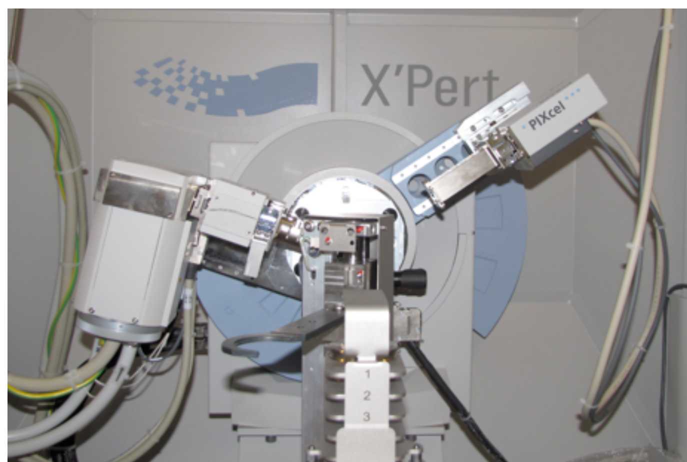

Figure 3.9: PANalytical X'Pert PRO Multi-Purpose X-Ray Diffractometer used for the XRD measurements

3.2.1.2 X-Ray Photoelectron Spectroscopy

X-ray photoelectron spectroscopy (XPS) is a technique used to determine the chemical state of the sample surface. Monochromatic X-rays are used to radiate the sample. Photoelectrons occur due to this irradiation and a certain photon escape from the sample surface. The binding energy of these electrons is determined using an electron energy analyzer (Figure 3.10). Intensity and binding energy of photoelectrons reveal the atomic composition, chemical state and electronic state of the sample. Binding energy can be calculated using the following equation:

$$E_{binding} = E_{photon} - (E_{kinetic} + W)$$

where E_{photon} is the energy of the incident photons, $E_{kinetic}$ is the kinetic energy of the photoelectron and W is the work function of the spectrometer.

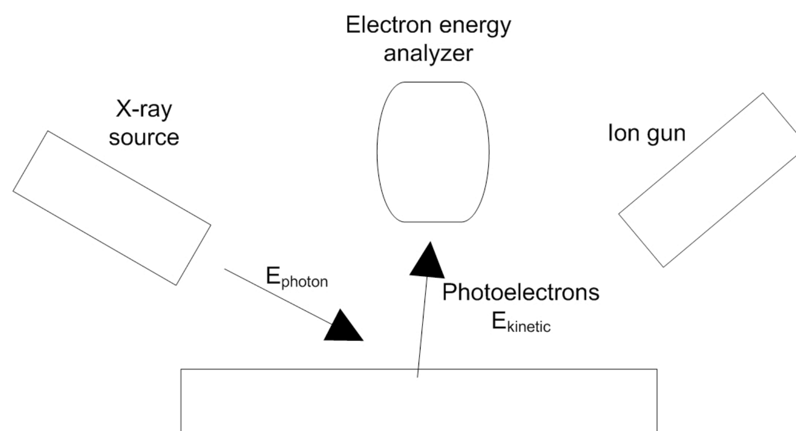

Figure 3.10: Schematic representation of the basic components of X-ray photoelectron spectroscopy.

In this study, Thermo Scientific K-Alpha spectrometer was used (Figure 3.11). Al Kα radiation is used in this system for irradiating the surface.

Figure 3.11: Thermo Scientific K-Alpha X-Ray photoelectron spectroscopy system.

Although XPS is a surface characterization technique, whole depth of the film could be analyzed by etching the sample with ion gun. In this work, sample surface is etched with Ar ions in order to obtain atomic concentrations of the elements present throughout the bulk film. Acceleration voltage and spot size of the air ions are 1 kV and 400 μm, respectively.

3.2.1.3 Scanning Electron Microscopy

The scanning electron microscope (SEM) focuses a beam of electrons onto the surface of the sample. The interaction of these electrons with the surface produces electrons (back-scattered electrons and secondary electrons) and X-rays. Generally there are separate detectors for detecting each of them. Secondary electrons are used to form the image of the surface. Heavy atoms scatter more strongly than light atoms. This principle in mind, back-scattered electrons are used to generate images with compositional information. X-rays are used for elemental analysis. For the inspection of ZnO surface, FEI Nova NanoSem 430 scanning electron microscope was used (Figure 3.12).

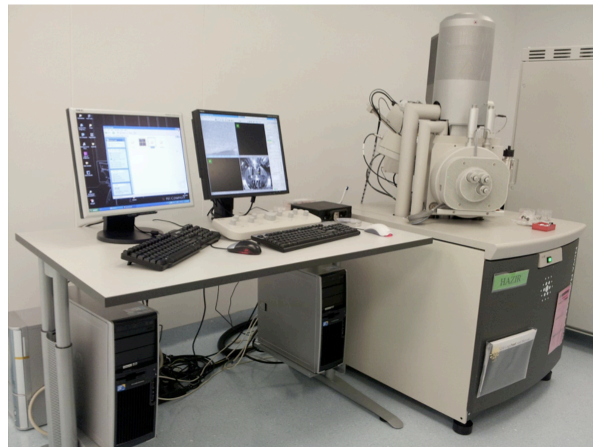

Figure 3.12: Nova-NanoSem scanning electron microscope.

3.2.1.4 Transmission Electron Microscopy

In a transmission electron microscope (TEM), an electron beam is transmitted through a very thin specimen. The image is formed using the transmitted electrons. High resolution TEM (HRTEM) is used to obtain images with atomic resolution and selected area electron diffraction (SAED) can be used to provide crystallographic information.

In this work, HRTEM of the ZnO films were obtained using FEI Tecnai G2 F30 TEM (Figure 3.13). ZnO films were prepared for TEM examination using FEI Nova 600i Nanolab focused ion beam (FIB) system. Using FIB ZnO was thinned with ions and Pt was used as a holder.

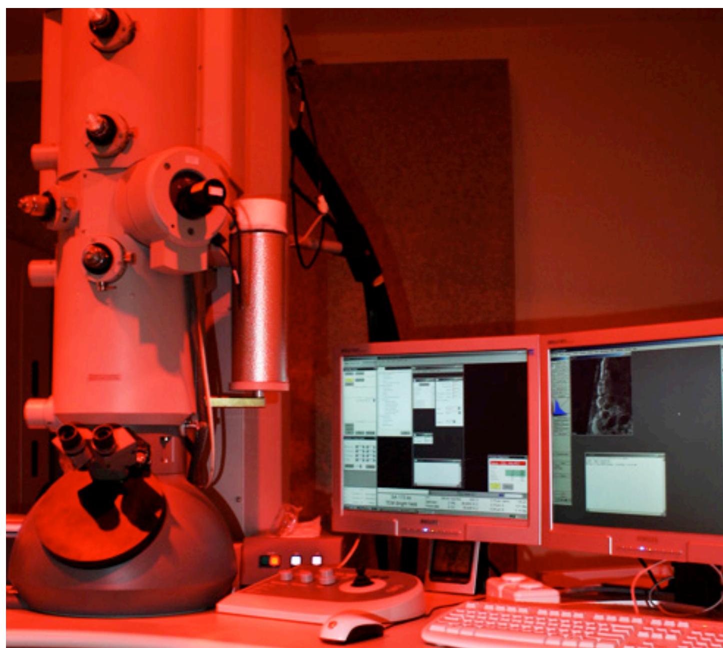

Figure 3.13. FEI Tecnai G2 F30 transmission electron microscope.

3.2.1.5 Spectroscopic Ellipsometry

Ellipsometry measures the change in polarization of light after it is reflected or transmitted from the sample. Amplitude ratio (ϕ) and phase difference (∇) are used to describe the change in polarization. Optical properties and thickness of the film affect the change in polarization, hence ellipsometry is used mainly for thickness and optical constant determination. Composition, crystallinity, roughness, doping concentration are some of the other properties that can be obtained using ellipsometry.

In this work, Variable Angle Spectroscopic Ellipsometer (VASE©) made by J.A. Woolam Co. (Figure 3.14) was used to determine thicknesses and optical constants of the ZnO films. Measurements were done using three angles of

incidence 65°, 70° and 75° within a wavelength range of 450-1200 nm. Cauchy dispersion function was used for modeling optical constants and film thickness estimation.

Figure 3.14: J.A. Woolam Co. V-VASE spectroscopic ellipsometer.

3.2.1.6 Atomic Force Microscopy

Atomic force microscope (AFM) is a type of scanning probe microscope in which images are generated by the physical interaction of a probe with the sample surface. Resolution of AFM is lower than 1 nm. Dominant interaction mechanism between the AFM tip and the surface is Van der Waals forces. These forces deflect the cantilever and this deflection is measured using a laser system (Figure 3.15). The relation between the amount of the deflection and the sample surface is realized using Hooke's law

$$F = -kx$$

where force, F, needed to extend or compress a spring with a stiffness, k, by a distance, x.

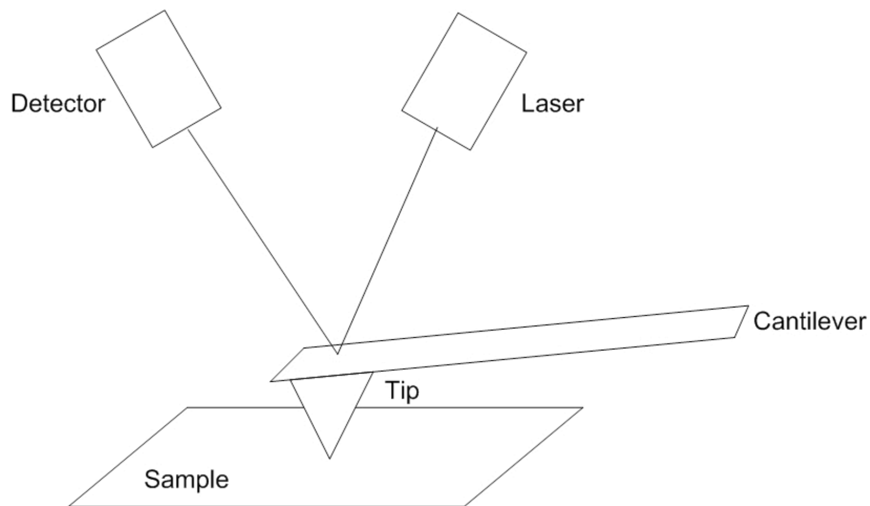

Figure 3.15: Schematic representation of how tip movements are detected typically in AFM.

For studying the surface of ZnO thin films, PSIA XE-100E atomic force microscope was used in contact mode (Figure 3.16).

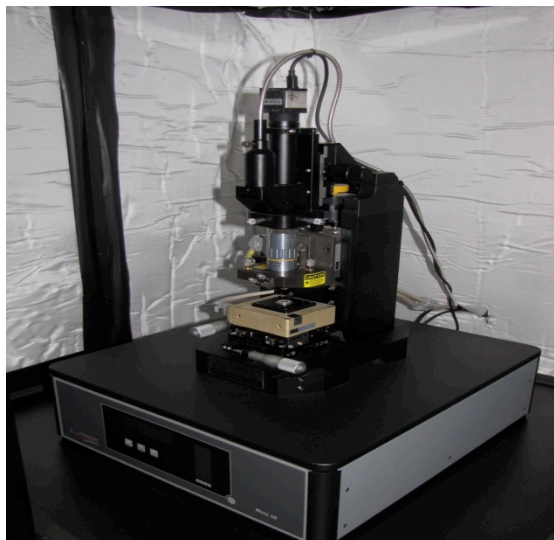

Figure 3.16: PSIA XE-100E atomic force microscope used for the morphological characterization of ZnO films.

3.2.2 SAW Device Characterization

For the characterization of SAW devices Network Analyzer was used. Network Analyzer is a device which is used to measure scattering parameters (s-parameters) of two-terminal devices. SAW delay line is also a two-port device where each IDT is a single terminal.

The main components of a network analyzer include a signal generator, a test set and a receiver. Signal generator, generates the signal used to test the device. Test set transfers this signal to the device. Then it delivers the signal back to the receiver in order to perform amplitude and phase calculations.

In a two port device, there are four scattering parameters: S_{11}, S_{12}, S_{21}, S_{22}. Basically they define the ratio of voltage out to voltage in. Consider a signal incident on one port. Part of the signal will be reflected back and part of the signal will be applied to the device under test. S_{11} measures the ratio of reflected signal to the signal incident on the port-1. Similarly S_{22} measures the ratio of reflected signal to the signal incident on the port-2. S_{12} and S_{21} are the parameters which measure the effectiveness of the signal transmission from one port to the other. Consider a signal is emitted from port 1 and reach port 2. S_{21} is the ratio of signal reaching port 2 to the signal generated from port 1. S_{12} is the ratio of signal reaching port 1 to the signal generated by port 2.

Figure 3.17 shows a two-port network scheme. a_1, a_2, b_1, b_2 are the signals approaching and leaving ports in the shown directions.

Figure 3.17: Schematic two-port network.

Following matrix equation shows the relation between incident signals and outgoing signals in terms of s-parameters.

$$\begin{bmatrix} b_1 \\ b_2 \end{bmatrix} = \begin{bmatrix} S_{11} & S_{12} \\ S_{21} & S_{22} \end{bmatrix} \begin{bmatrix} a_1 \\ a_2 \end{bmatrix}$$

In the SAW delay line, transmission from port 1 to port 2 is accomplished by acoustic waves. Therefore S_{21} parameter should be used as the measure of successful acoustic wave transmission for SAW devices.

In network analyzer measurements, insertion loss vs. frequency is the critical parameter that is measured. Relation between insertion loss (dB) and S_{21} is given by the following equation:

$$IL = 20\log_{10}|S_{21}|$$

Agilent Technologies E5071C Network Analyzer (300kHz-20GHz) and E8361A Network Analyzer (10MHz-67GHz) were used for the measurement of SAW delay lines fabricated in this work. Before the measurements, calibration should be performed in order to minimize systematic errors. Figure 3.18 shows how calibration should be performed using the calibration kit provided with the network analyzer. Load shown as the black square is 50 Ω. Figure 3.19 shows how to perform each calibration step.

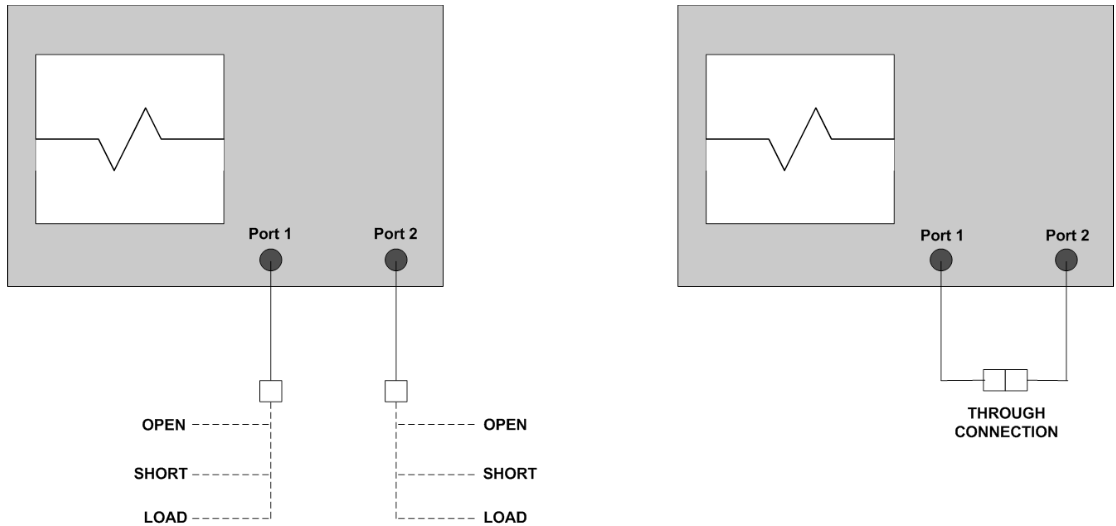

Figure 3.18: A scheme showing calibration steps. The order is not important.

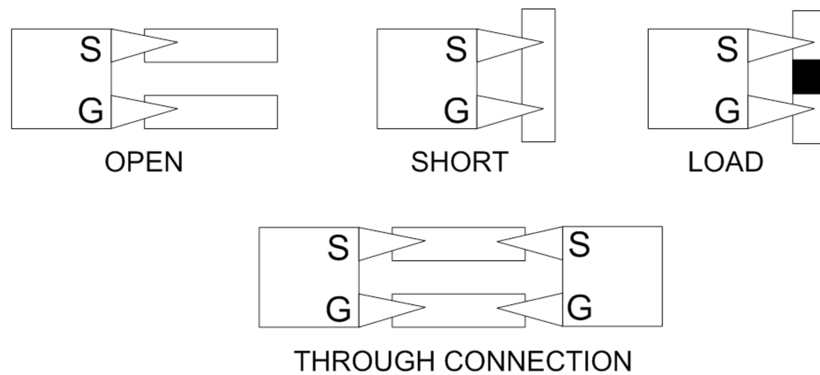

Figure 3.19: A figure depicting each calibration step. Black square is 50 Ω.

After calibration, actual device measurements were performed. Figure 3.20 shows how measurements were performed schematically. Figure 3.21 shows the actual measurement setup.

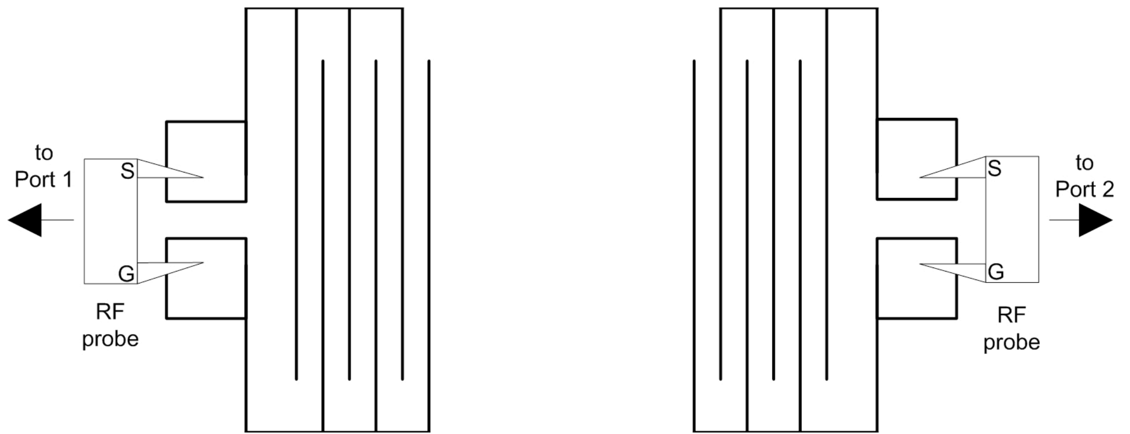

Figure 3.20: Schematic illustration of the measurement.

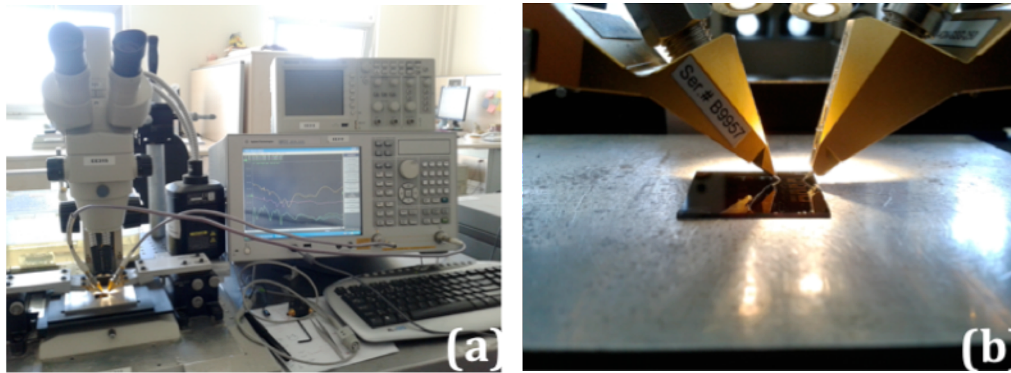

Figure 3.21: Actual measurement setup showing network analyzer (E5071C) and the probe station (a), RF probes and the device under test can be seen in (b).

Chapter 4

Results and Discussion

In this section, optimization of deposition parameters for improving c-axis orientation in ZnO films was presented and characterization results of optimized ZnO films were given. Effect of post deposition annealing on ZnO was also discussed. The chapter concludes with SAW device performance characterization.

4.1 Optimization and Characterization of ZnO

Before fabricating SAW devices using ZnO as the piezoelectric layer, the optimization of deposition parameters and characterization of optimized ZnO thin films was performed. The performance of the SAW devices strongly depends on the properties of the piezoelectric films (Chapter 2). Therefore, ZnO material characterization and optimization of material properties are necessary to improve device response.

4.1.1 Optimization of Deposition Parameters

As analyzed in Chapter 2, c-axis preferred orientation of ZnO grains provides the piezoelectricity of the film. Before fabricating SAW devices, deposition parameters of ZnO were optimized to improve c-axis orientation. XRD radial

scans were used to study texture. XRD measurements of the ZnO films revealed only one peak between the range 20°-70° which is the diffraction from the basal plane. This shows that basal plane is parallel to the surface and there exist no other planes oriented parallel to the surface. Therefore, optimization of the deposition parameters was concentrated on the improvement of this texture. From the XRD data, integrated intensity of the peak is calculated which is proportional to the diffracted volume. In order to compare films with different thicknesses, integrated intensity per unit film thickness is calculated by dividing the integrated intensity to film thickness. Deposition parameters such as deposition temperature, RF power and chamber pressure were optimized to maximize the integrated intensity per unit thickness (i.e. c-axis orientation).

4.1.1.1 Deposition Temperature

Three different temperatures, room temperature (RT), 100°C, and 200°C, were used to examine the effect of deposition temperature on texture. Other deposition parameters were held constant as 150 W RF power, 10 mTorr chamber pressure and 50 sccm Ar flow. Radial scans of the 0002 reflections of these films are presented in Figure 4.1 and from this data integrated intensity per unit thickness (i.e. 1 nm) is calculated and tabulated in Table 4.1.

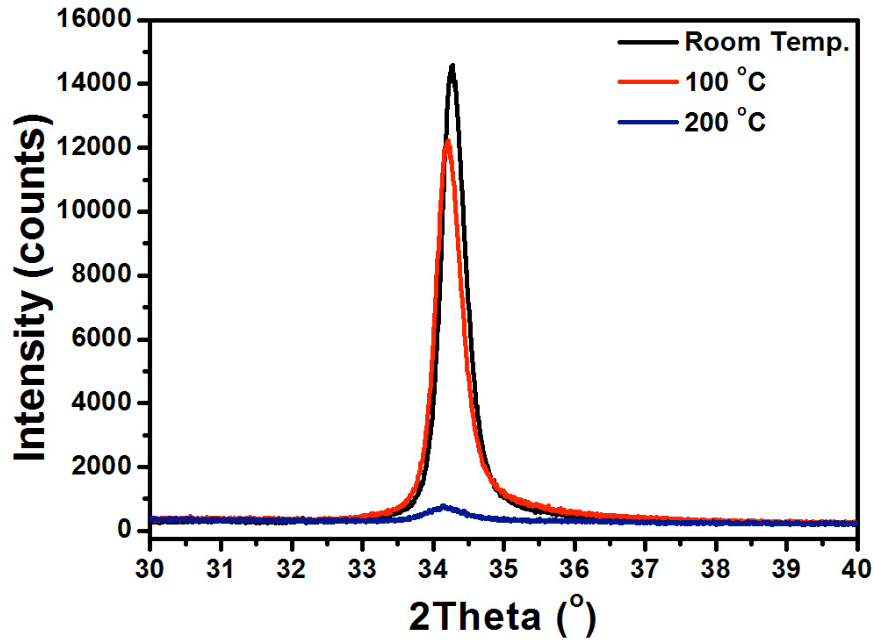

Figure 4.1: Radial scans of the 0002 reflections for the films deposited at three different temperatures.

Table 4.1: Integrated intensity values with respect to different deposition temperatures.

Deposition Temperature	RT	100°C	200°C
Integrated Intensity/nm	12.04 ± 0.13	10.53 ± 0.15	0.66 ± 0.06

From these results, it can be deduced that increasing deposition temperature hinders c-axis orientation. This result contradicts with the results reported in the literature where it is stated that increasing deposition temperature improves texture [11, 46]. The possible cause for this contradiction may be the discrepancy between conventional heating systems and the heating system utilized by VAKSIS sputtering system. In conventional heating systems substrate is heated by heating substrate holder. However, this system uses a heater 5 cm distant from the substrate and heats the substrate by radiation. Therefore sputtered atoms travelling from the target to the substrate could absorb this radiation. Tetrahedral formation of Zn and O atoms occur during

travelling between the target and the substrate. This absorbed radiation could hinder tetrahedral formation which could be the reason for texture deterioration. In conclusion, room temperature is the optimum deposition temperature for this system.

4.1.1.2 Deposition Power

In order to study the effect of RF power on preferred c-axis orientation, depositions were carried out with RF power settings of 75, 100 and 150 W. Chamber pressure and Ar flow were fixed to 10 mTorr and 50 sccm, respectively. Depositions were carried at room temperature. The results of the radial scans of the 0002 reflections are given in Figure 4.2 and integrated intensity values for unit thickness are listed in Table 4.2.

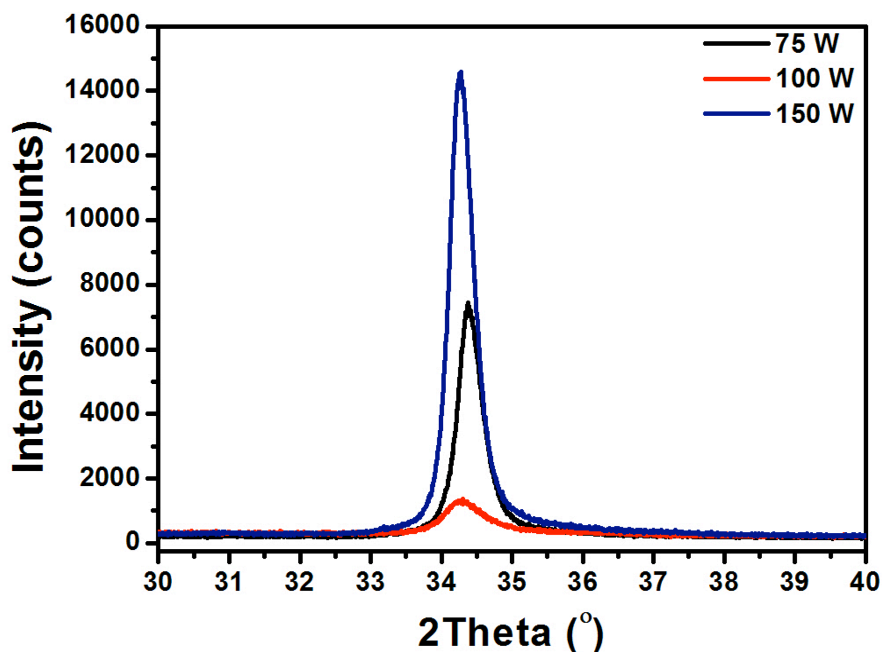

Figure 4.2: Radial scans of the 0002 reflections for the films deposited under three different rf power values.

Table 4.2: Integrated intensities per unit thickness for different RF power values.

RF Power	75 W	100 W	150 W
Integrated Intensity/nm	11.28 ± 0.16	2.68 ± 0.19	12.04 ± 0.13

There is no linear trend in this data. Depositions were conducted twice in order to prevent erroneous data, still results were the same. More data points are needed in order to be sure that the trend is parabolic. Deposition power has two opposing effects on c-axis orientation. First, as the deposition power increases sputtered atoms become more energetic. This will assist atoms to find their lowest possible energy sites by surface diffusion, results in the preferred c-axis orientation. Secondly, however, deposition power increases the rate of deposition. Atoms need time and energy to reach their lowest energy sites. Increased rate of deposition decreases the time available for atoms to move freely therefore c-axis orientation could be hindered [46, 47]. These two opposing forces may be the reason for this assumed parabolic trend. Nevertheless, 150 W was selected to be the deposition power for the ZnO thin-films used to fabricate SAW devices.

4.1.1.3 Chamber Pressure

Another important parameter to optimize is the chamber pressure. Depositions at chamber pressures of 5, 10 and 20 mtorr were carried out at nominally room temperature, 100 W RF power and 50 sccm Ar flow to study this dependency. For the resulting three films, radial scans of the 0002 reflections are given in Figure 4.3 and integrated values per unit thickness are tabulated in Table 4.3.

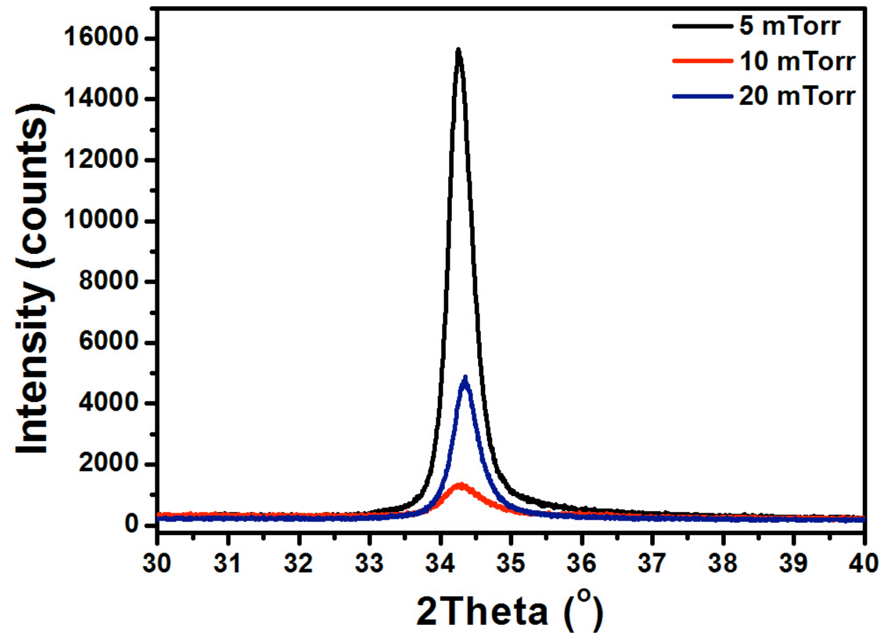

Figure 4.3: Radial scans of the 0002 reflections for film deposited at different chamber pressures.

Table 4.3: Integrated intensities per unit thickness for the films deposited using three different chamber pressures.

Chamber Pressure	5 mTorr	10 mTorr	20 mTorr
Integrated Intensity/nm	23.09 ± 0.44	2.71 ± 0.18	10.31 ± 0.20

Among the parameters worked out, 5 mtorr is the optimum chamber pressure during depositions. Again, the trend is not linear, integrated intensity per unit thickness of the film deposited with the chamber pressure 10 mtorr seems to be a false data due to rapid decrease but deposition repetition confirmed the data. In the literature it is stated that low chamber pressures are advantageous for c-axis orientation [46, 48] because as the chamber pressure decreases the sputtered atoms traveling from the target to the substrate will encounter less collisions with the sputtering gas atoms hence target atoms will arrive to the substrate with higher energy. As noted in the preceding section, more atoms will find their equilibrium positions because they have higher energy. Chamber pressure of 5 mtorr is used for the depositions hereafter.

Ar/O ratio is the only deposition parameter which is not optimized during this work to increase the c-axis orientation. In the literature it is stated that using Ar alone as a sputtering gas causes Zn rich films. Zn surplus, in other words oxygen deficiency, increases the conductivity which lessens the piezoelectricity. Adding O_2 into the sputtering gas eliminates this problem by increasing the oxygen content in the film. [11, 47].

In light of the abovementioned facts, ZnO sputtering deposition recipe used in this work is tabulated in Table 4.4.

Table 4.4: ZnO deposition recipe determined for the VAKSIS RF magnetron sputtering system.

Deposition Temperature	RF Power	Chamber Pressure	Ar Flow	O_2 Flow
RT	150 W	5 mTorr	50 sccm	10 sccm

4.1.2 Characterization of ZnO

Optimized ZnO thin films were further characterized in terms of their morphology, crystal structure, composition and optical properties. First, surface morphology and cross-section of the ZnO thin film were examined using SEM (Figure 4.4).

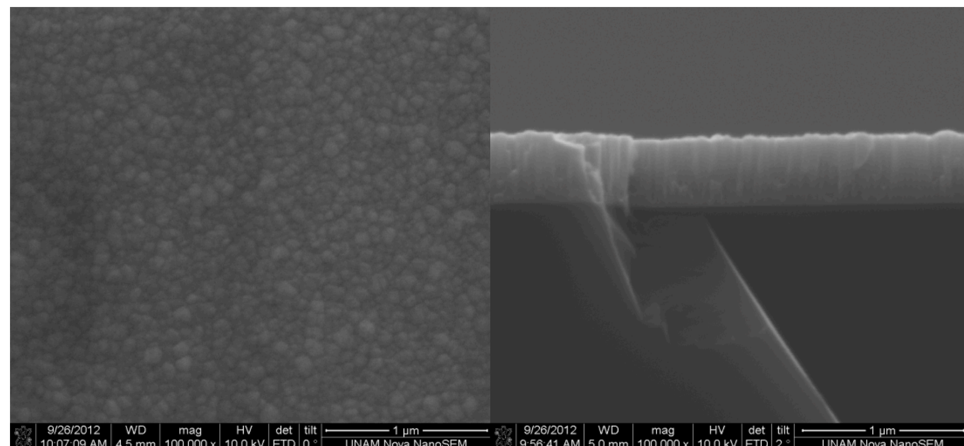

Figure 4.4: SEM image of the (a) surface and (b) cross section of the sputtered 402 nm thick ZnO on Si wafer.

Growth of columnar structures in the thin film is apparent from these images. TEM image of the film cross-section reveals its crystalline structure (Figure 4.5).

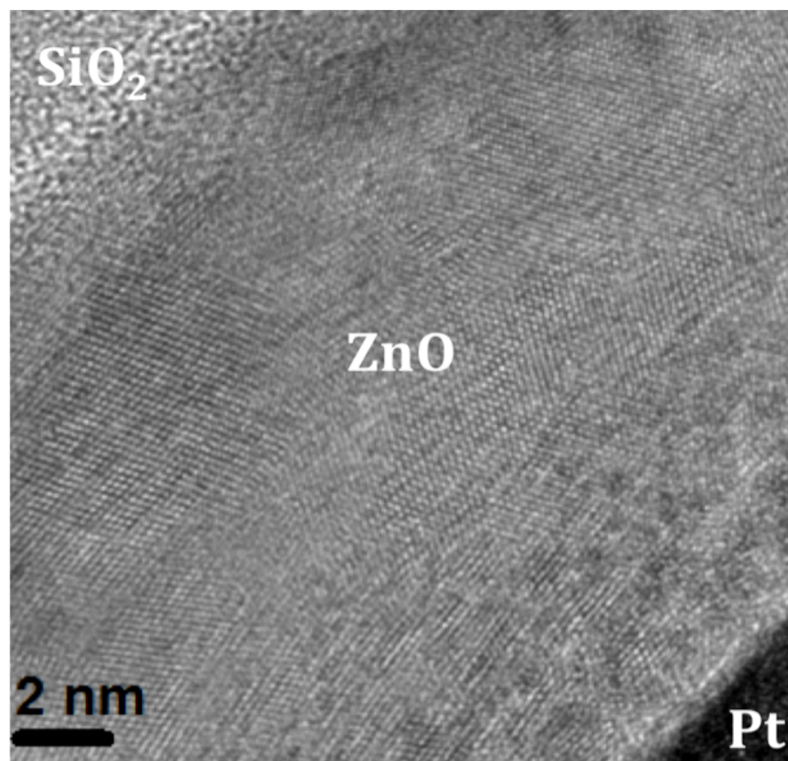

Figure 4.5: TEM image of the ZnO cross section. SiO_2 is the native oxide of the silicon wafer while Pt is the holder coated during sample preparation.

XPS was used to study the chemical compositions and bonding states of the deposited ZnO thin films. Survey scans detected peaks of zinc (Zn), oxygen (O), and carbon (C) with the concentrations of ~50.4, ~49.2, and ~0.4, at.%, respectively from the bulk film. Concentrations were calculated by averaging the survey data at each 10 s etch level. There was an increase of the C and O at the surface which is most probably due to contamination and oxidation caused by ambient air exposure. Depth profile measurement of the film was conducted to observe the uniformity of the elemental compositions towards the bulk film and is shown in Figure 4.6.

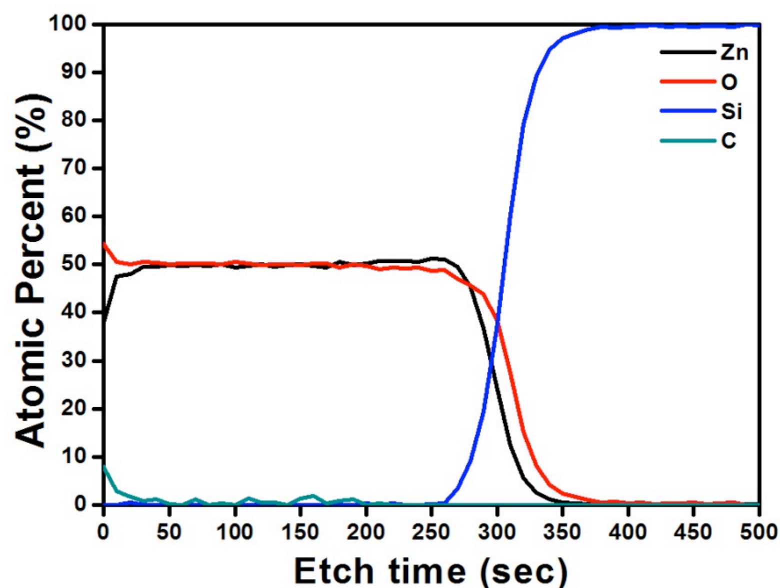

Figure 4.6: XPS depth profile analysis results of the ZnO thin film over silicon wafer showing the uniform composition throughout the bulk film.

Other than elemental composition studies, high resolution XPS scans were performed to study the bond structure of the ZnO thin film. Chemical states and the presence of any possible compositions were analyzed after fitting the high resolution spectra. In all XPS measurements, the binding energies have been calibrated by taking C1s peak (285 eV) as reference. Zn 2p high resolution XPS spectrum taken after 300 s Ar etch is given in Figure 4.7(a). The binding energies of 1021.14 and 1044.18 eV correspond to the doublet of Zn2p 3/2 and 1/2, respectively, as reported for ZnO [49]. Figure 4.7(b) shows the O 1s high resolution spectrum from the same region of the ZnO film. The peak centered at 529.85 eV (subpeak#1) is associated to the O^{2-} ion in the wurtzite structure surrounded by the Zn atoms. The peak with the lower intensity at 531.76 eV is attributed to the presence of OH bonds as reported in the literature [50].

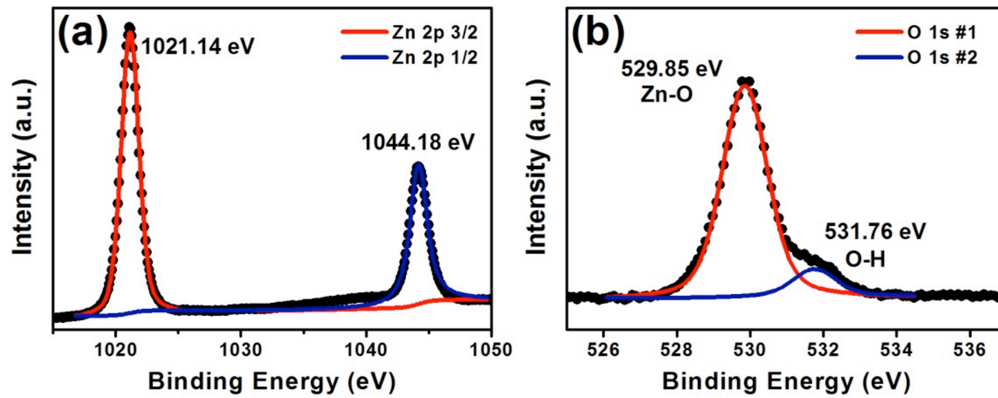

Figure 4.7: (a) Zn 2p and (b) O 1s high resolution XPS spectra of the optimized ZnO thin film after 300 s of Ar etch.

AFM is used to determine the surface roughness of the ZnO films. Topographic image obtained using AFM is given in Figure 4.8. Root mean square (RMS) roughness is calculated as 0.99 nm.

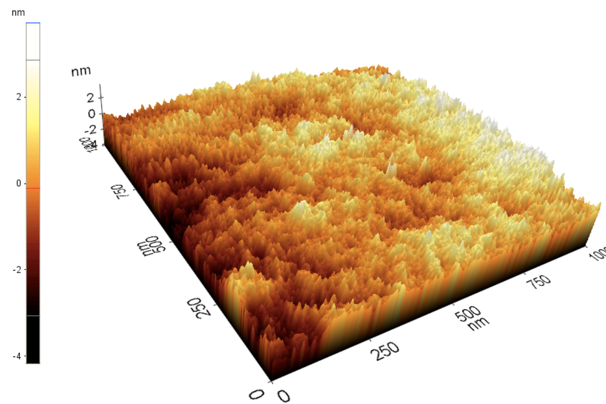

Figure 4.8: AFM image of sputtered ZnO over silicon wafer.

Thicknesses and optical constants of the ZnO films were obtained using spectroscopic ellipsometry. Ellipsometric spectra of the films were measured within the wavelength range of 450-1200 nm and modeled by Cauchy dispersion function using (0.5mm) Si/ ZnO layer structure. The refractive indices of the ZnO film was found as 2.06 and 1.91 for the wavelengths of 450 and 1200 nm, respectively which is in agreement with those reported in literature [51]. Figure 4.9 represents the fitted data of 207.5 nm-thick ZnO film.

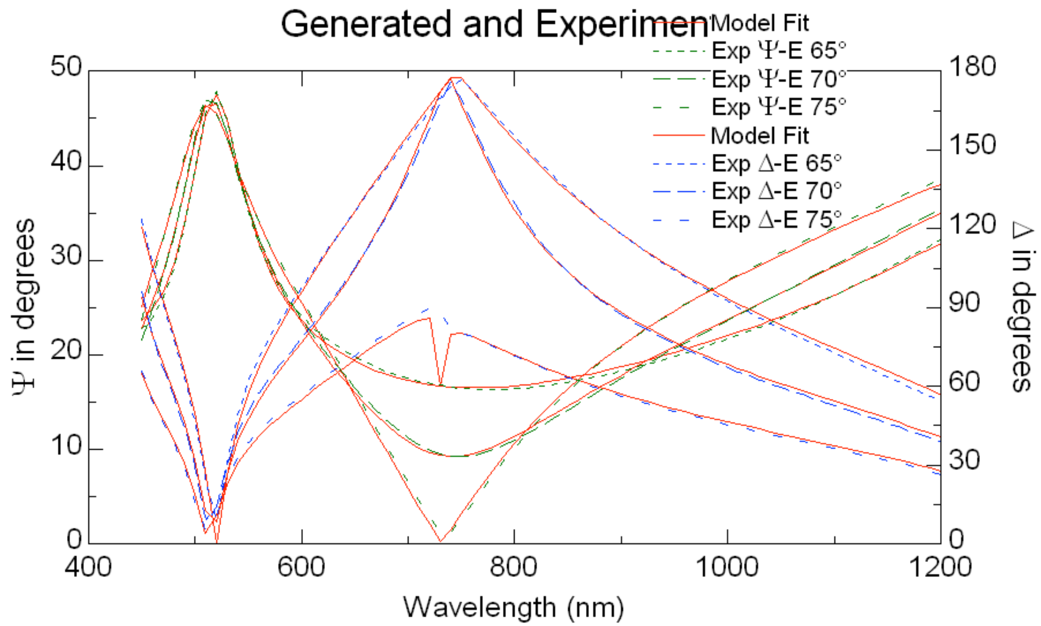

Figure 4.9: Fitting data of the ZnO film using Cauchy dispersion function to obtain thickness and refractive index values.

4.1.3 Post-deposition Annealing

In this section, effect of post-deposition annealing on the structure of ZnO film is studied. In the literature it is stated that c-axis orientation increases as the annealing temperature increases [52]. To prove this claim, characterization of ZnO films annealed at different temperatures is presented in this part. In the following section, effect of annealing temperature on SAW device performance will be shown and results will be interpreted in the light of the structure revealed in this section.

To study the effect of annealing, 207.5 nm thick ZnO film was sputtered, with the parameters stated in Table 4.4, on Si wafers and cut into pieces to perform the annealing at temperatures 400°C, 500°C, 600°C, 700°C, 800°C, 900°C and 1000°C for 30 min. Following annealing, films were characterized using XRD, AFM, SEM and ellipsometry. Figure 4.10 shows the radial scans of the 0002 reflections of the films with respect to different annealing

temperatures. Integrated intensity per unit thickness for these films are given in Table 4.5. In Figure 4.10, Bragg angle for the 0002 reflection, 34.42° [53], of a powder sample is also shown in order to compare the residual stress in the films.

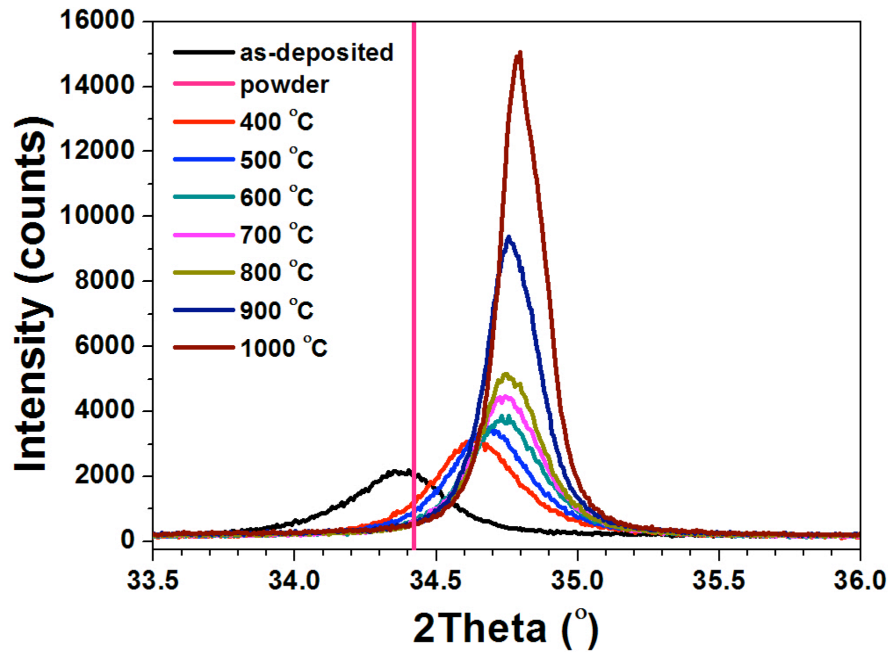

Figure 4.10: Radial scans of the 0002 reflections for the as-deposited and annealed films.

Table 4.5: Integrated intensity per unit thickness and full width at half maximum values according to annealing temperatures.

Annealing Temperature	None	400°C	500°C	600°C	700°C	800°C	900°C	1000°C
Integrated intensity/nm	4.78 ±.10	5.13 ±.12	5.21 ±.16	6.05 ±.21	6.19 ±.15	6.22 ±.13	9.46 ±.13	13.54 ±.31
FWHM(°)	.39 ± .13E-3	.34 ± .14E-3	.32 ± .18E-3	.30 ± .13E-3	.28 ± .16E-3	.25 ± .96E-4	.21 ± .75E-4	.18 ± .10E-3

From these data it can be deduced that as the annealing temperature increases integrated intensity per unit thickness increases. This implies texture improvement with increasing annealing temperatures. Another important property, peak broadening (i.e. FWHM) decreases as the annealing temperature

increases which indicates grain growth in the direction perpendicular to the surface in accordance with Scherrer's equation [10].

One last property to deduce from the data above is the stress in the film. Bragg angle for the 0002 plane in the powder is given as 34.42°. As-deposited film has a Bragg angle ($34.36° \pm 0.63$E-3) lower than the powder. Due to Bragg's law, this means that interplanar spacing, d, for the planes (0002) are larger than the unstressed value. This indicates residual stress with compressive components perpendicular to the c-axis. This stress is investigated by various groups and it is found that impacting sputtering atoms and interstitial atoms are the cause for the stress [54]. When the films are annealed, interplanar spacing, d_{0001}, decreases below its unstressed value. This indicates a tensile stress parallel to the c-axis, and it increases as the annealing temperature increases. This is caused by plastic flow in the film at elevated temperature. The thermal expansion coefficient (α) of silicon is 2.5 x 10^{-6}/°C and for the ZnO crystal α_{11} and α_{33} are 6.05 and 3.53 x 10^{-6}/°C, respectively [55]. Thus, when the films are cooled back down, it shrinks more than the substrate and is placed in tension.

AFM measurements were performed in order to determine change in the RMS roughness values of the films after annealing. Figure 4.11 shows RMS roughness of ZnO films with respect to different annealing temperatures.

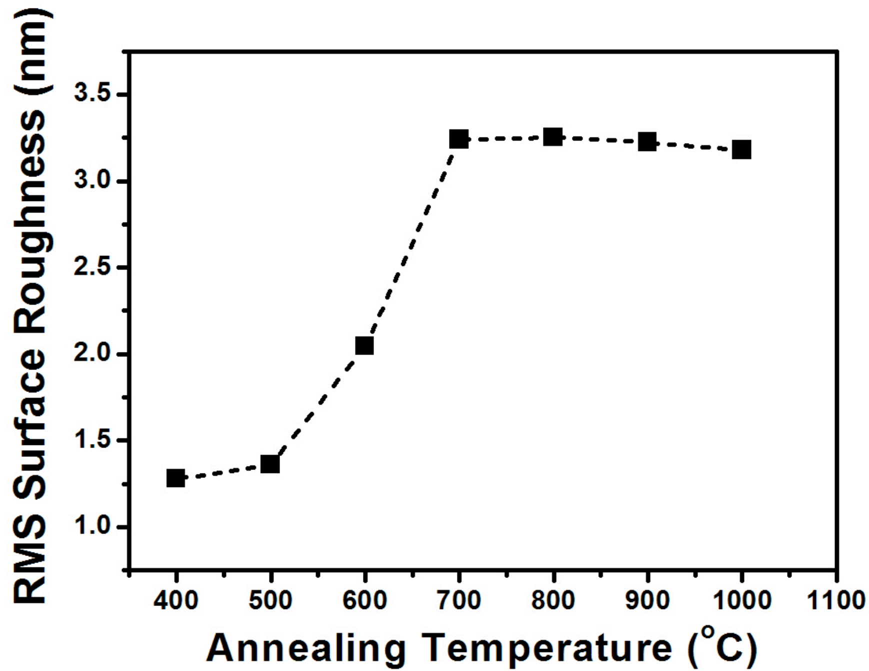

Figure 4.11: RMS surface roughness values of the films annealed at different temperatures. Error values are smaller than the height of the data points.

Figure 4.11 shows that although roughness change is minor below 500°C and after 700°C, it increases very sharply between 500°C and 700°C. This indicates the occurrence of a structure change between these temperatures. ZnO films are further characterized to obtain information about this structure change.

Refractive index is a parameter dependent on crystallinity of the material which means that a change in crystal structure affects the refractive index. Therefore, a refractive index change is expected due to the structure change deduced from the AFM data. The refractive indices of the films annealed at different temperatures were measured using spectroscopic ellipsometry and presented in Figure 4.12.

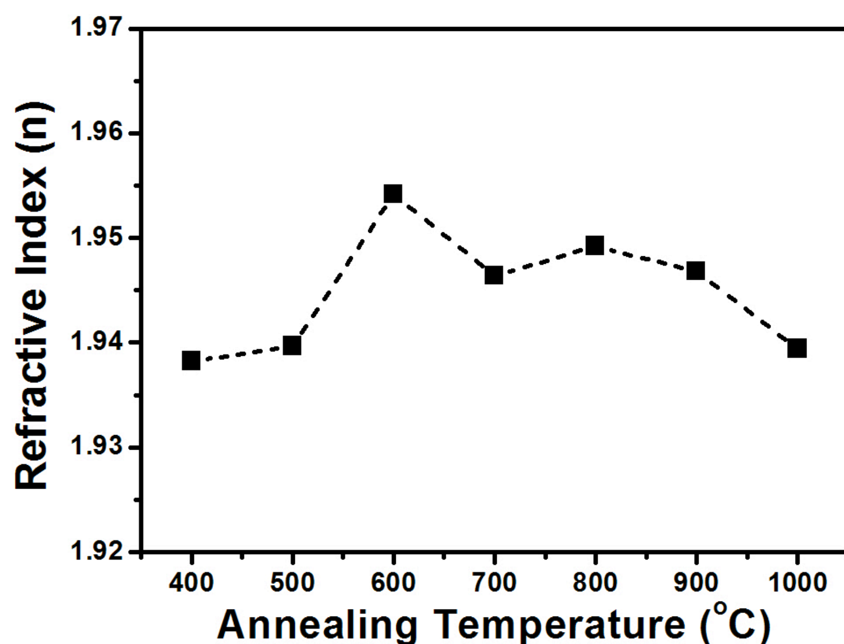

Figure 4.12: Refractive index of the films annealed at different temperatures. Error values are smaller than the height of the data points.

Refractive index increases with annealing temperature until 600°C reaching its maximum value. Further annealing at higher annealing temperatures decreases the refractive index. This data is in good agreement with the data obtained by AFM. The refractive index increases until 600°C and an event predicted by the rapid roughness increase occurs after 600°C causing refractive index to decrease. SEM images of the films annealed at 600°C and 1000°C are taken to further study the morphology and is shown in Figure 4.13.

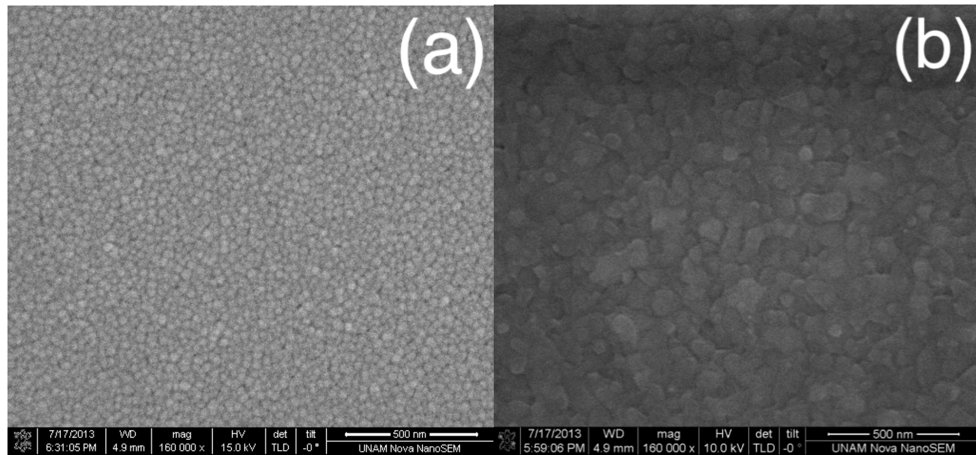

Figure 4.13: SEM image of the ZnO surface annealed at (a) 600°C and (b) 1000°C.

By comparing two figures, grain growth can be seen. There is also another point to note. Grains are different not just in their dimensions but also in their morphologies. This is probably related with the predicted structure change.

In the literature, the structural change upon annealing above 600°C discussed so far is presented as coalescence of small crystallites to form larger crystallites [52, 54]. It is stated that this causes major grain growth resulting in microcracks, porosity and surface roughness. Two different annealing temperatures were noted for the occurrence of this change which were 400°C [52] and 600°C [54]. In Ref. [52], it is stated that surface roughness is the dominant factor causing attenuation in SAW devices therefore annealing ZnO at elevated temperatures are not suitable for SAW devices.

Puchert et al. showed that decreasing annealing time without changing the annealing temperature decreases surface roughness of ZnO films [56]. To validate this claim, ZnO is annealed at 600°C and 1000°C for 5 min and Figure 4.14 shows its roughness value. In addition, XRD pattern of the films annealed for 5 and 30 min at 1000°C are presented in order to examine the effect of annealing time on texture (Figure 4.15).

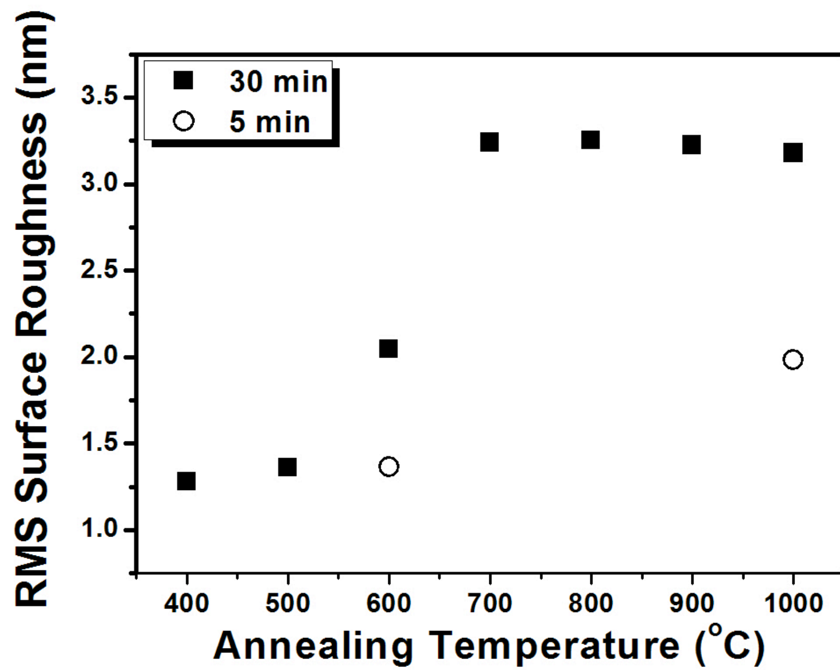

Figure 4.14: RMS surface roughness vs. Annealing temperature graph for annealing durations 5 and 30 min.

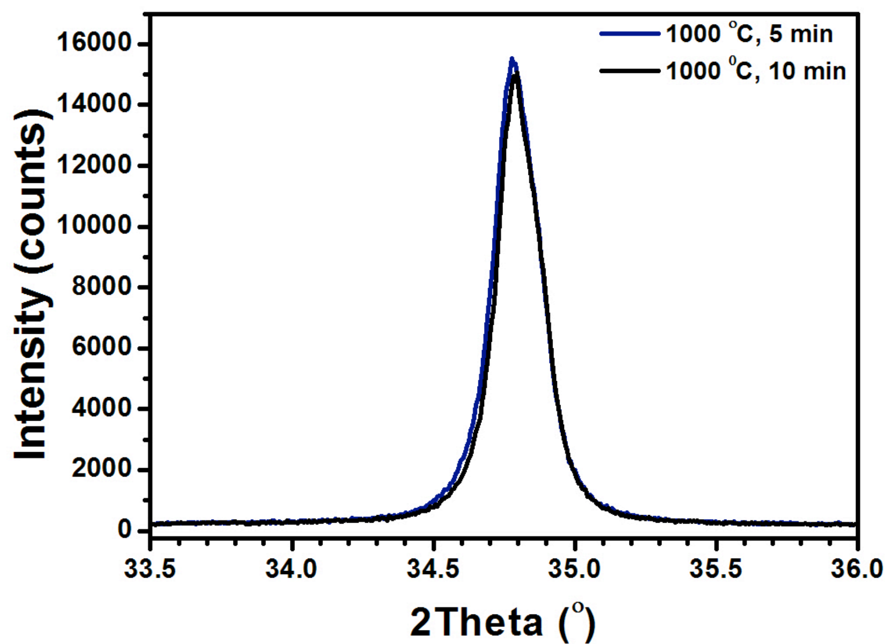

Figure 4.15: Radial scans of the 0002 reflections for the films annealed at 1000°C for 5 and 30 min.

It can be seen that roughness decreases with shorter annealing durations without compromising texture improvement. ZnO film annealed at 1000°C for 5 min has a roughness even below the film annealed at 600°C for 30 min. This information will be used to test the effect of roughness on SAW device performance in the following section.

In summary, as annealing temperature increases texture improves and roughness increases. For the SAW performance, texture improvement is favorable whereas surface roughness hinders device performance due to increased surface attenuation (sec 2.2.3). Also after 600°C, according to literature, coalescence of crystallites occur causing roughness, porosity and microcracks [52, 54].

4.2 Characterization of SAW Devices

In this part, effect of the several fabrication parameters on the SAW device response is presented. The influence of ZnO annealed at different temperatures for different durations on SAW device performance will be introduced first. Then, effect of the insertion of SiO_2 layer between the substrate and the piezoelectric film will be shown followed by the effect of ZnO thickness. In this study, IDT structure was not considered as a variable. IDT finger width and spacing were equal to 5 μm (i.e λ=20 μm) with a propagation length of 65 μm and an aperture of 1600 μm. Number of finger pairs were 30. As the IDT material, 100 nm gold was used with 3 nm titanium as an adhesive layer.

4.2.1 Effect of Annealing

In Section 4.1.3, characterization of ZnO films annealed at different temperatures were presented. In this section, effect of annealing on the device performance will be shown. For that purpose, 1305 mm thick ZnO was

deposited on a silicon wafer with the optimized recipe given in Table 4.4. Substrate was cut into seven pieces and they were annealed in N_2 atmosphere with different durations and temperatures shown in Table 4.6. Agilent Technologies E8361A Network Analyzer was used to measure insertion loss (S_{21}) vs. frequency responses of the devices were measured using network analyzer and presented in Figure 4.16.

Table 4.6: Annealing parameters for ZnO.

Temperature (°C)	400	600	600	800	800	1000	1000
Time (min)	30	5	30	5	30	5	30

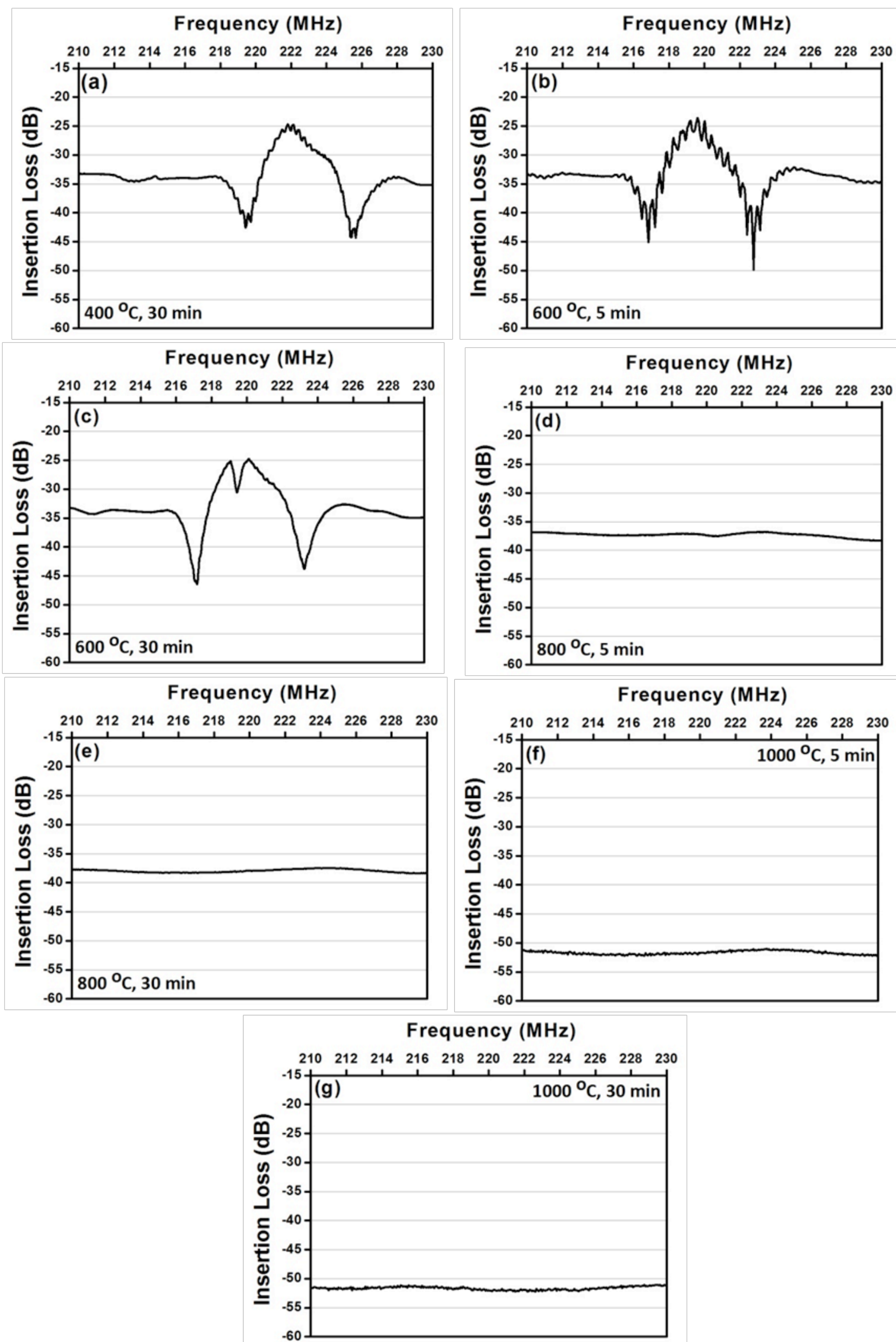

Figure 4.16: Response of the SAW devices utilizing ZnO annealed at (a) 400°C for 30 min, (b) 600°C for 5 min, (c) 600°C for 30 min, (d) 800°C for 5 min, (e) 800°C for 30 min, (f) 1000°C for 5 min and (g) 1000°C for 30 min.

These results reveal that SAW devices utilizing the films annealed at 800°C and above are not working despite the fact that the texture of the films are improved as the annealing temperature increases.

As explained in the preceding section, one of the reasons behind this performance decrease is given as the surface roughness in the literature [52]. It is stated that as the annealing temperature increases, surface roughness of the ZnO thin films increases, and this causes SAW wave traveling between two IDTs to scatter, and hence attenuate until reaching the output IDT.

However, from the results presented in Figures 4.16 (a)-(e), it can be deduced that roughness is not the cause for the decrease in performance. It is shown in section 4.1.3 that decreasing annealing time decreases surface roughness while retaining the improved texture. ZnO annealed at 600°C for 30 min is rougher than the ZnO annealed at 1000°C for 5 min (Figure 4.14). Still, SAW device utilizing the ZnO annealed at 600°C for 30 min outperforms the device utilizing the ZnO annealed at 1000°C for 5 min which is not even responding. Figure 4.16 (c) and (f).

Figure 4.17 (combination of Figure 4.16 (b) and (c)) shows the response of the SAW devices fabricated using ZnO annealed at 600°C for 5 and 30 mins. Although the film annealed for 30 min is rougher, there is no apparent change in the response of the device. This shows that attenuation due to roughness increase is minute if not zero for these roughness values.

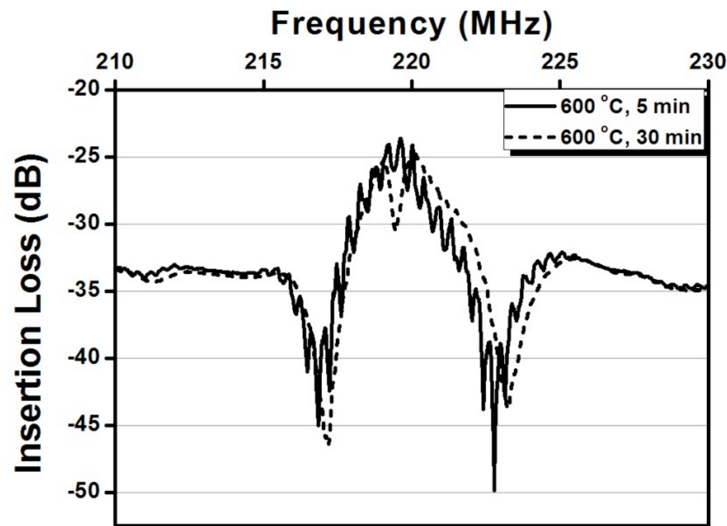

Figure 4.17: Insertion loss vs. frequency response of the devices utilizing ZnO annealed at 600°C for 5 and 30 min.

Therefore, dominant mechanism for device breakdown is not rapid roughness increase as opposed to the conventional wisdom. The breakdown is probably related with the coalescence of crystallites. As stated before coalescence results in roughness, porosity and microcracks. Hence either porosity or microcracks (or both) cause device breakdown due to coalescence of crystallites.

Phan and Chung [57] fabricated SAW resonators with ZnO film annealed at 400-600-800-1000°C. They found that the optimum temperature is 600°C. They explain the hindered device performance for 800°C and 1000°C with the formation of cracks and increase in roughness and residual stress.

Different optimum annealing temperatures for ZnO were reported by several groups can be listed as: 400°C (1h) [58] 480°C (1h) [59] 600°C (1h) [57] and 1000°C (5 min) [56].

4.2.2 Effect of SiO_2 Interlayer

In the literature it is stated that adding a SiO_2 layer between ZnO and Si increases the acoustic energy confinement at the surface of the devices which increases electromechanical coupling coefficient [60, 61].

In order to study the effect of SiO_2 addition, two devices were fabricated. One of them utilized 50 nm of rf-sputtered SiO_2 between ZnO and Si the other did not. ZnO thickness was ~1890 nm for both of the devices. Frequency dependence of S_{21} parameter for both devices were measured using Agilent Technologies E5071C Network Analyzer and presented in Figure 4.18.

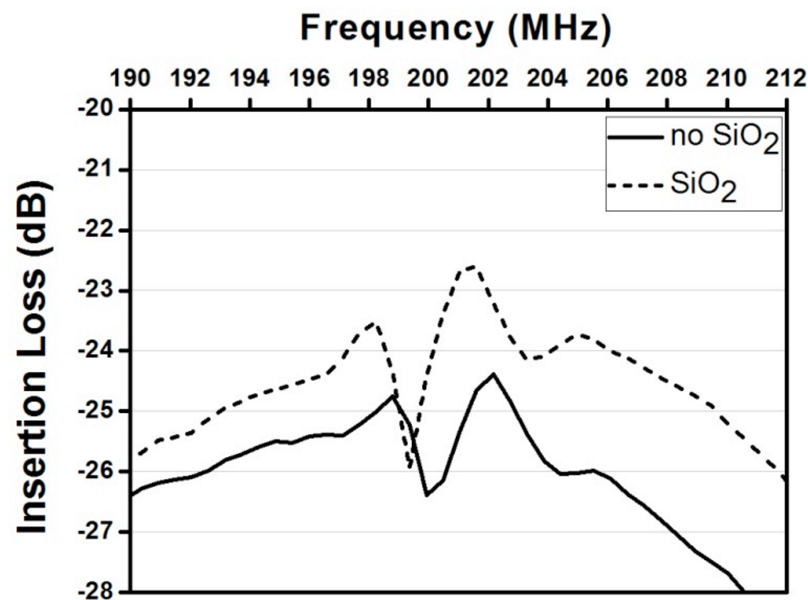

Figure 4.18: Effect of SiO_2 addition on SAW device response.

It is apparent from the figure that the effect of SiO_2 addition is significant. Insertion loss at the central frequency decreases from 24.4 dB to 22.6 dB. Central frequency shifts from 202.2 MHz to 201.6 MHz with the insertion of SiO_2.

4.2.3 Effect of Film Thickness

Two devices with ~1890 nm and ~1560 nm ZnO layers were fabricated. Figure 4.19 shows S_{21} vs frequency response for both devices measured using Agilent Technologies E5071C Network Analyzer.

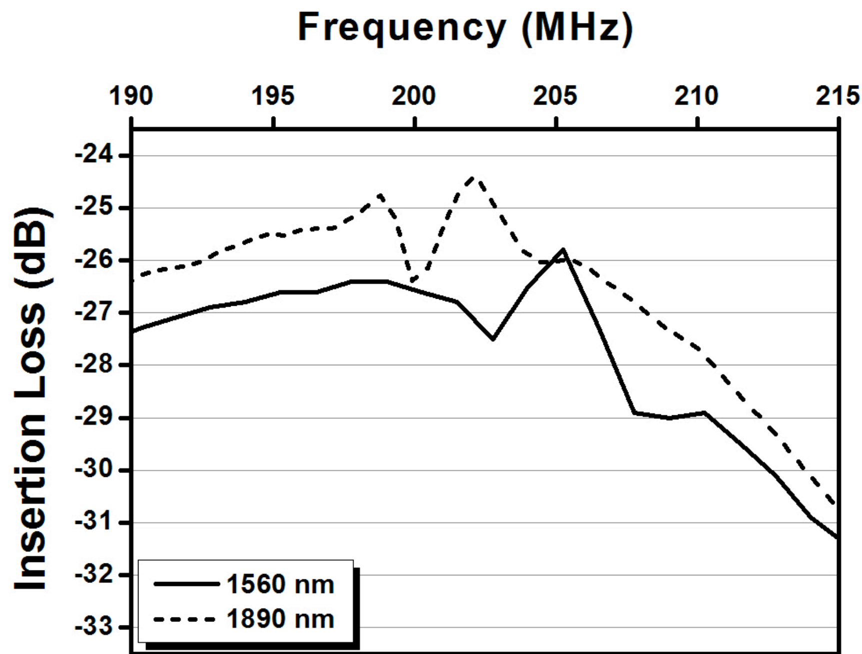

Figure 4.19: Insertion loss vs frequency response of the devices utilizing 1560 and 1890 nm thick ZnO.

When compared with 1560 nm film, 1890 nm thick ZnO results in less insertion loss and frequency shift.

Chapter 5

Conclusions and Future Directions

In this study, sputtering parameters of ZnO films were optimized in order to increase c-axis orientation. This would increase the piezoelectricity of ZnO, hence increase the SAW device performance utilizing this film.

In addition, effect of annealing on the properties of ZnO films and device performance was studied. It is revealed that devices utilizing ZnO films annealed above 600°C deteriorates. In the literature, it is widely noted that roughness increase due to annealing results in scattering of SAWs and that is the primary reason for device breakdown. In this study, it is shown that roughness increase is not the mechanism causing device breakdown. To prove this claim, two devices utilizing ZnO films annealed at 600°C for 30 min and at 1000°C for 5 min were fabricated. ZnO films annealed at 1000°C for 5 min has lower roughness than the one annealed at 600°C for 30 min. Nevertheless the device utilizing the more rough film outperforms the device utilizing the less rough film. Also there was no apparent performance difference between the devices utilizing films annealed at 600°C for 5 and 30 min although their roughnesses were different. We can safely claim that roughness alone is not the main reason for the SAW device breakdown.

Effect of SiO_2 interlayer addition was also investigated within the scope of this thesis. It was found out that addition of SiO_2 layer increases the device performance as also suggested in the literature. Finally, the effect ZnO thickness on device performance is noted and it was showed up that best device performance is obtained using 1.89 µm thick ZnO film among others.

There are two main paths to follow after this study. First one is to improve the performance of the SAW device further and the second one is to fabricate functional SAW sensors. For the first path, a setup to measure piezoelectricity, or d_{33} alone, should be established. By this way, assumptions could be tested. In recipe optimization, it is assumed that improved c-axis orientation will result in better SAW device performance. However, this assumption rules out the effect of other phenomena occurring during the process. As proved in annealing studies, although orientation improves as the annealing temperature rises, devices breakdown after annealing at 600°C. Another way to follow up this study is to investigate the effect additional layer on SAW device performance. In this study, one material with one thickness deposited with one method (SiO_2-50nm-sputtering). For example, SiO_2 can be deposited via PECVD or can be grown via thermal oxidation. As another layer material, Al_2O_3 could be studied which can be deposited using sputtering and ALD. IDT dimensions were fixed in this work, however it can be an area of another parametric study on its own. For example propagation length for the devices fabricated at this work was 65 µm. Its effect on device performance should be studied because firstly it determines the time delay of the device and secondly for sensor applications it defines the amount of the active area. Effect of IDT materials, metal thickness, metallization ratio and finger thickness on device performance could also be investigated.

After completing the optimization of SAW device, SAW chemical sensors could be studied. Initially a SAW device with palladium film over the delay line may be fabricated for H_2 sensing. Measurement setup should also be modified in

order to measure the effect of H_2 in real time. For biological sensing, configuration of the device should be changed because Rayleigh waves attenuate under liquid loading and majority of biological measurements are done in liquid environments.

Bibliography

[1] W.G. Cady, *Piezoelectricity,* McGraw-Hill Book Company, 1946.

[2] J. Curie and P. Curie, "Development by pressure of polar electricity in hemihedral crystals with inclined faces," *Bull. Soc. Min. de France*, vol. 3, pp. 90-93, 1880.

[3] W. G. Hankel, "Piezoelektrischen Eigenschaften Des Bergkrystalles," *Ber. Sachs.,* vol. 33, pp. 52-63, 1881.

[4] G. Lippmann, "Principle of the Conservation of Electricity," *J. phq.*, vol. 10, pp. 381-394, 1881.

[5] J. Curie and P. Curie, "Dilatation electrique du quartz," *J. Phys. Theor. Appl.*, Vol. 8, pp. 149-168, 1881.

[6] L. Kelvin, "On the piezoelectric property of quartz," *Phil. Mag.*, vol. 36, pp. 331-453, 1893.

[7] W. Voigt, "General theory of the piezo- and pyroelectric properties of crystals," *Abh. Gött.* vol. 36, pp. 1-99, 1890.

[8] L. Langevin and A. Moulin, "Sur la variation du module du quartz en fonction de la température," *J. Phys. Radium*, vol. 8, pp. 257-259, 1937.

[9] S. Tasaka et al., "Structure and properties of amorphous piezoelectric vinylidene cyanide copolymers," *Polymer,* vol. 30, pp. 1639-1642, 1989.

[10] B. D. Cullity, *Elements of X-ray Diffraction*, Prentice Hall, 1979.

[11] N. Fujimura et al., "Control of preferred orientation for ZnO_x films: control of self-texture," *J. Cryst. Growth,* vol. 130, pp. 269-279, 1993.

[12] M. J. Madou, *Fundamentals of Microfabrication :The Science of Miniaturization.* Boca Raton, FL: CRC Press, 2001.

[13] U. Ozgur et al., "A comprehensive review of ZnO materials and devices," *J. Appl. Phys.,* vol. 98, pp. 041301-103, 2005.

[14] N. Emanetoglu et al., "Epitaxial ZnO piezoelectric thin films for saw filters," *Materials Science in Semiconductor Processing,* vol. 2, pp. 247-252, 1999.

[15] H. Wohltjen and R. Dessy, "Surface acoustic wave probe for chemical analysis. I. Introduction and instrument description," *Anal. Chem.,* vol. 51, pp. 1458-1464, 1979.

[16] M. Thompson and D. C. Stone, *Surface-Launched Acoustic Wave Sensors: Chemical Sensing and Thin-Film Characterization.* Wiley New York, 1997.

[17] L. Rayleigh, "On waves propagated along the plane surface of an elastic solid," *Proceedings of the London Mathematical Society,* vol. 1-17, pp. 4-11, 1885.

[18] D'Amico and E. Verona, "Saw sensors," *Sensors and Actuators,* vol. 17, pp. 55-66, 5/3, 1989.

[19] H. Weber, G. Weiss and S. Hunklinger, "Comparison of rayleigh and sezawa wave modes in ZnO-SiO_2-Si structures," in *Ultrasonics Symposium Proceedings., IEEE,* 1991, pp. 363-366 vol.1.

[20] D. Hauden, G. Jaillet and R. Coquerel, "Temperature sensor using SAW delay line," in *Ultrasonics Symposium,* 1981, pp. 148-151.

[21] H. Scherr et al., "Quartz pressure sensor based on SAW reflective delay line," in *Ultrasonics Symposium Proceedings. IEEE,* 1996, pp. 347-350 vol.1.

[22] G. Maugin, "Shear horizontal surface acoustic waves on solids," in *Recent Developments in Surface Acoustic Waves*, Springer, 1988, pp. 158-172.

[23] R. M. White and F. W. Voltmer, "Direct piezoelectric coupling to surface elastic waves," *Appl. Phys. Lett.,* vol. 7, pp. 314-316, 1965.

[24] C. Auguste, "Surface acoustic Wave (SAW) devices: Technologies and global markets," BBC Research, Tech. Rep. IAS039A, 2012.

[25] F. S. Hickernell, "Surface acoustic wave devices: A rewarding past, a significant present, and a promising future," in *Microwaves and Radar MIKON.,* 1998, pp. 159-168 vol.4.

[26] H. Wohltjen and R. Dessy, "Surface acoustic wave probe for chemical analysis. I. Introduction and instrument description," *Anal. Chem.,* vol. 51, pp. 1465-1470, 1979.

[27] M. T. Fertsch, "A surface acoustic wave vapor sensing device," M.S. thesis, Dept. Elect. Eng., U.C. Berkeley, Berkeley, CA, 1980.

[28] A. Bryant et al., *A Surface Acoustic Wave Gas Detector,* Maine Univ. Orono, 1982.

[29] M. C. Horrillo et al., "Optimization of SAW sensors with a structure ZnO–SiO2–Si to detect volatile organic compounds," *Sensors Actuators B: Chem.,* vol. 118, pp. 356-361, 10/25, 2006.

[30] M. J. Fernández et al., "Discrimination of volatile compounds through an electronic nose based on ZnO SAW sensors," *Sensors Actuators B: Chem.,* vol. 127, pp. 277-283, 10/20, 2007.

[31] D'Amico, A. Palma and E. Verona, "Hydrogen sensor using a palladium coated surface acoustic wave delay-line," in *Ultrasonics Symposium,* 1982, pp. 308-311.

[32] V. B. Raj et al., "Cross-sensitivity and selectivity studies on ZnO surface acoustic wave ammonia sensor," *Sensors Actuators B: Chem.,* vol. 147, pp. 517-524, 6/3, 2010.

[33] K. Nicolae, C. Viespe and C. Grigoriu, "Nanocomposite sensitive polymeric films for SAW sensors deposited by the MAPLE direct write technique," *Sensors Actuators B: Chem.,* vol. 158, pp. 418-422, 11/15, 2011.

[34] M. T. Moy et al., "Atrazine measurements using surface transverse wave devices," *Anal. Chem.,* vol. 67, pp. 1510-1516, 1995.

[35] J. Kondoh et al., "Enzyme-immobilized SH-SAW biosensor," *Sensors Actuators B: Chem.,* vol. 20, pp. 199-203, 6, 1994.

[36] M. Gaso Rocha, Y. Jiménez, F. A. Laurent and A. Arnau (2013). Love Wave Biosensors: A Review, State of the Art in Biosensors - General Aspects, Dr. Toonika Rinken (Ed.), ISBN: 978-953-51-1004-0, InTech, DOI:10.5772/53077.

[37] G. Tsortos et al., "Quantitative Determination of Size and Shape of Surface-Bound DNA Using an Acoustic Wave Sensor," *Biophys. J.,* vol. 94, pp. 2706-2715, 4, 2008.

[38] E. Howe and G. Harding, "A comparison of protocols for the optimisation of detection of bacteria using a surface acoustic wave (SAW) biosensor," *Biosensors and Bioelectronics,* vol. 15, pp. 641-649, 12, 2000.

[39] S. Krishnamoorthy et al., "An interleukin-6 ZnO/SiO2/Si surface acoustic wave biosensor," *Biosensors and Bioelectronics,* vol. 24, pp. 313-318, 10/15, 2008.

[40] S. J. Martin et al., "SAW resonators on silicon," in *Ultrasonics Symposium,* 1982, pp. 290-294.

[41] S. J. Martin et al., "Surface acoustic wave resonators on a ZnO-on-Si layered medium," *Journal of Applied Physics,* vol. 54, pp. 561-569, 1983.

[42] R. Asai, O. Takeshi, and M. Shoichi, "Rayleigh surface-acoustic-wave device using ZnO (0001)/SiO_2/Si (111)[11]," U.S. Patent No. 4,562,371, 1985.

[43] S. Seo, W. Shin and J. Park, "A novel method of fabricating ZnO/diamond/Si multilayers for surface acoustic wave (SAW) device applications," *Thin Solid Films,* vol. 416, pp. 190-196, 9/2, 2002.

[44] J. Lee et al., "Effects of lattice mismatches in ZnO/substrate structures on the orientations of ZnO films and characteristics of SAW devices," *Thin Solid Films,* vol. 447–448, pp. 296-301, 1/30, 2004.

[45] X. Y. Du et al., "ZnO film for application in surface acoustic wave device," *Journal of Physics: Conference Series,* vol. 76, pp. 012035, 2007.

[46] F. S. Hickernell, "Zinc Oxide Films for Acoustoelectric Device Applications," *IEEE Transactions on Sonics and Ultrasonics,* vol. 32, pp. 621-629, 1985.

[47] J. Molarius et al., "Piezoelectric ZnO films by r.f. sputtering," *Journal of Materials Science: Materials in Electronics,* vol. 14, pp. 431-435,

[48] F. C. M. van de Pol, F. R. Blom and T. J. A. Popma, "R.f. planar magnetron sputtered ZnO films I: Structural properties," *Thin Solid Films,* vol. 204, pp. 349-364, 10/10, 1991.

[49] C. Wagner and G. Muilenberg, *Handbook of X-Ray Photoelectron Spectroscopy.* Perkin-Elmer, 1979.

[50] L. Yang et al., "Origin of the surface recombination centers in ZnO nanorods arrays by X-ray photoelectron spectroscopy," *Appl. Surf. Sci.,* vol. 256, pp. 3592-3597, 2010.

[51] S. Mishra et al., "Study on optical properties of Sputter deposited ZnO thin films on Silicon," *ICOP*, vol. 33, pp. 55-60, 2009.

[52] V. Gupta and A. Mansingh, "Influence of postdeposition annealing on the structural and optical properties of sputtered zinc oxide film," *J. Appl. Phys.,* vol. 80, pp. 1063-1073, 1996.

[53] JCPDS Card No. 80-0075

[54] Z. B. Fang et al., "Influence of post-annealing treatment on the structure properties of ZnO films," *Appl. Surf. Sci.,* vol. 241, pp. 303-308, 3/15, 2005.

[55] J. Jou, M. Han and D. Cheng, "Substrate dependent internal stress in sputtered zinc oxide thin films," *Journal of Applied Physics,* vol. 71, pp. 4333-4336, 1992.

[56] M. K. Puchert, P. Y. Timbrell and R. N. Lamb, "Postdeposition annealing of radio frequency magnetron sputtered ZnO films," *Journal of Vacuum Science & Technology A: Vacuum, Surfaces, and Films,* vol. 14, pp. 2220-2230, 1996.

[57] G. Phan and G. Chung, "The effect of post-annealing on surface acoustic wave devices based on ZnO thin films prepared by magnetron sputtering," *Appl. Surf. Sci.,* vol. 257, pp. 4339-4343, 2/15, 2011.

[58] S. Chu, W. Water and J. Liaw, "Influence of postdeposition annealing on the properties of ZnO films prepared by RF magnetron sputtering," *Journal of the European Ceramic Society,* vol. 23, pp. 1593-1598, 9, 2003.

[59] Z. B. Fang et al., "Influence of post-annealing treatment on the structure properties of ZnO films," *Appl. Surf. Sci.,* vol. 241, pp. 303-308, 3/15, 2005.

[60] S. J. Ippolito, "Investigation of multilayered surface acoustic wave devices for gas sensing applications," PhD. thesis, Dept. of Elec. Eng., RMIT Univ., Melbourne, 2006.

[61] R. Srivastava and A. Mansingh, "Surface acoustic wave transduction in the ZnO-SiO_2-Si structure," *J. Phys. D,* vol. 21, pp. 1535, 1988.